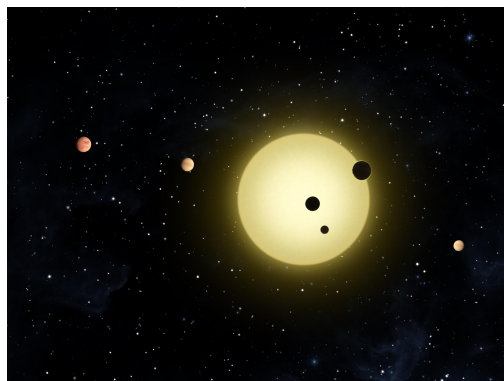Aristotle University of Thessaloniki
Faculty of Science
Department of Physics
Section of Astrophysics, Astronomy and Mechanics
Laboratory of Astronomy

Diploma Thesis:

Detection of an additional extra-solar planet and simulation of perturbations on transit light-curves

Angelos Tsiaras

Supervisor:
Professor John H. Seiradakis

With data from
Kepler Mission
and
Holomon Astronomical Station

Thessaloniki, July 2014

Ευχαριστίες

Περίληψη

Από την ανακάλυψη του πρώτου πλανήτη εκτός του ηλιακού μας συστήματος το 1992 μέχρι και σήμερα, ο αριθμός των εξω-πλανητών έχει αυξηθεί ραγδαία ξεπερνώντας του 1700. Οι περισσότεροι από αυτούς έχουν ανακαλυφθεί με τη μέθοδο των διαβάσεων (transit), της πτώσης δηλαδή του φωτός των αστέρων που τους φιλοξενούν όταν παρεμβάλλονται ανάμεσα σε αυτούς και τη Γη. Πέραν, όμως, των ίδιων των εξωπλανητών τα τελευταία χρόνια έχει αυξηθεί σημαντικά και ο αριθμός εξω-πλανητικών συστημάτων, ειδικά με τη βοήθεια των καμπυλών φωτός του διαστημικού προγράμματος Kepler. Η ανακάλυψη και η μελέτη αυτών των συστημάτων είναι πιθανό στο μέλλον να μας δώσει απαντήσεις σε ερωτήματα που αφορούν το δικό μας ηλιακό σύστημα και γι' αυτό θεωρείται σημαντική και έχει τραβήξει την προσοχή μεγάλου μέρους της επιστημονικής κοινότητας. Στην παρούσα εργασία θα μελετήσουμε την καμπύλη φωτός ενός αστέρα που περιέχει διάβαση αλλά, κυρίως, θα ασχοληθούμε με δύο φαινόμενα που την αλλοιώνουν και οφείλονται στην παρουσία ενός επιπλέον πλανήτη στο ίδιο πλανητικό σύστημα. Πιο συγκεκριμένα, τα φαινόμενα αυτά είναι η διπλή διάβαση, κατά την οποία δύο πλανήτες ευθυγραμμίζονται και ο ένας αποκρύπτει τον άλλο, και οι διαταραχές στην περιοδικότητα μίας διάβασης που προκαλεί ένας επιπλέον, "αόρατος", πλανήτης. Τα δεδομένα που θα χρησιμοποιήσουμε προέρχονται από το διαστημικό πρόγραμμα Kepler και από δικές μας παρατηρήσεις και φωτομετρία από τον αστρονομικό σταθμό Χολομώντα του Αριστοτελείου Πανεπιστημίου.

Abstract

Since the discovery of the first planet outside our solar system (exo-planet) in 1992, the number of exo-planets has grown rapidly, surpassing 1700. Most of them have been discovered with the method transits, meaning the drop in the flux of their host stars when inserted between them and the earth. Apart from the number of exo-planets in recent years the number of exo-planetary systems has increased significantly too, especially through the analysis of the light-curves of the space program Kepler. The discovery and study of these systems is likely in the future to give us answers to questions concerning the formation, the structure and the evolution of planetary systems, including our own. In this thesis we model the transit light-curve and the overlapping double transit light-curve and apply them on light-curves of multi-transiting exo-planetary systems from the Kepler mission. Additionally, we try to detect TTVs in light-curves of single-transiting exo-planets from the Kepler mission and announce some new TTV candidates. TTVs are variations in the time of a transit and in most cases they are caused by gravitational perturbations of other exo-planets in the same exo-planetary system. Finally we set up a new follow-up program in order to detect TTVs in light-curves of other known single-transiting exo-planets from the Holomon Astronomical Station of the Aristotle University of Thessaloniki. For this purpose we develop a photometry code and a Monte Carlo fitting code in order to fit our transit light-curve model on our data.

Contents

Σύνοψη

Το πρώτο κεφάλαιο αποτελεί μία εισαγωγή στην πορεία της εξερεύνησης των έξω-ηλιακών πλανητών από τις αρχές του 1990 μέχρι και σήμερα. Αναφέρονται δε και κάποιες από τις βασικές μεθόδους ανίχνευσης έξω-ηλιακών πλανητών όπως είναι η μέθοδος των ακτινικών ταχυτήτων, η μέθοδος του βαρυτικού μικρο-φακού και η μέθοδος των διαβάσεων. Επιπλέον, γίνεται αναφορά και στον ολοένα και αυξανόμενο αριθμό γνωστών έξω-ηλιακών συστημάτων. Η ανίχνευση τέτοιων συστημάτων γίνεται είτε άμεσα, με την παρατήρηση παραπάνω της μίας διάβασης στην καμπύλη φωτός του ίδιου αστέρα, είτε έμμεσα, με την παρατήρηση διαταραχών σε μία καμπύλη διάβασης που προέρχονται από ένα τρίτο σώμα που τυχαίνει να μην κάνει διάβαση. Στην εργασία αυτή θα προσπαθήσουμε να ανιχνεύσουμε και να προσομοιώσουμε τέτοιου είδους φαινόμενα, που σχετίζονται δηλαδή με την παρουσία ενός πρόσθετου έξω-ηλιακού πλανήτη στο ίδιο σύστημα με έναν άλλο γνωστό από τις διαβάσεις του.

Για να ανιχνεύσουμε και να προσομοιώσουμε διαταραχές σε μία καμπύλη διάβασης θα πρέπει πρώτα να είμαστε σε θέση να την αναπαράγουμε υπολογιστικά. Η προσομοίωση της καμπύλης διάβασης αναλύεται στο δεύτερο κεφάλαιο. Αρχικά υπολογίζουμε την προβαλλόμενη πάνω στην ουράνια σφαίρα απόσταση αστέρα και πλανήτη με βάση τα εκτιμώμενα ή τα επιθυμητά στοιχεία της τροχιάς του, την περίοδο, την κλίση, τον μεγάλο ημι-άξονα, το όρισμα του περιηλίου και το μήκος του αναβιβάζοντα συνδέσμου. Στη συνέχεια αναλύουμε έναν υπολογιστικό τρόπο για τον σωστό υπολογισμό της πτώσης στο φως του αστέρα που θα προκαλεί κάθε φορά ο πλανήτης ανάλογα με την υπολογισμένη μεταξύ τους προβαλλόμενη απόσταση και τα στοιχεία του πλανήτη (την ακτίνα του) και του αστέρα (τις σταθερές αμαύρωσης του χείλους). Η αμαύρωση του χείλους είναι ένα φαινόμενο που κάνει τον αστέρα να μην φαίνεται ομοιόμορφα φωτισμένος, κάνοντας τον υπολογισμό ακόμη πιο περίπλοκο.

Στην συνέχεια, τρίτο κεφάλαιο, προσομοιώνουμε ένα φαινόμενο που έχει να κάνει με την ύπαρξη πρόσθετου πλανήτη που όμως και αυτό πραγματοποιεί διαβάσεις. Αυτό το φαινόμενο είναι η αλληλεπικάλυψη δύο πλανητών την ώρα της ταυτόχρονης διάβασης τους από τον αστέρα που τους φιλοξενεί. Και αυτή η προσομοίωση απαιτεί τα ίδια βήματα με πριν αλλά φυσικά η κατάσταση είναι αρκετά ποιο περίπλοκη όταν μπαίνει στο παιχνίδι και ένα τρίτο σώμα. Τέτοιες προσο-

μοιώσεις έχουν γίνει και στο παρελθόν αλλά η δική μας περιλαμβάνει όλες τις πιθανές περιπτώσεις αλληλεπικάλυψης των τριών σωμάτων και επομένως είναι πιο γενική. Θα θέλαμε πολύ να συμπεριλάβουμε και την διαταραχή που προκαλεί στην τροχιά του ενός πλανήτη ο άλλος αλλά αυτό ήταν πέραν των ορίων (κυρίως χρονικών) αυτής της πτυχιακής εργασίας. Έτσι, θεωρούμε απλά δύο προβλήματα των δύο σωμάτων και υπολογίζουμε τις προβαλλόμενες αποστάσεις όπως και στο προηγούμενο κεφάλαιο.

Το τελευταίο προπαρασκευαστικό κομμάτι πριν την μελέτη πραγματικών δεδομένων είναι να φτιάξουμε ένα πρόγραμμα που να μπορεί να εφαρμόζει τις θεωρητικά υπολογισμένες καμπύλες φωτός των κεφαλαίων δύο και τρία σε πραγματικά δεδομένα για να μπορούμε να πούμε ποιο σετ παραμέτρων αναπαράγει με τον καλύτερο τρόπο τα πραγματικά δεδομένα. Η διαδικασία αυτή είναι η γνωστή μας τεχνική των ελαχίστων τετραγώνων μόνο που εδώ τα μοντέλα δεν είναι γραμμικά οπότε δεν υπάρχουν αναλυτικοί τρόποι για βρούμε την καμπύλη ελαχίστων τετραγώνων. Για το λόγω αυτό εφαρμόζουμε, στο τέταρτο κεφάλαιο μία τεχνική μου λέγεται Monte Carlo fitting σύμφωνα με την οποία πρέπει να αναπαράγουμε πάρα πολλές καμπύλες φωτός, με διαφορετικό σετ αρχικών παραμέτρων και να ψάξουμε να βρούμε αυτήν που ταιριάζει καλύτερα.

Τα δύο τελευταία τελευταία κεφάλαια είναι το απόσταγμα των προηγούμενων καθώς αποτελούν την πειραματική επιβεβαίωση των μοντέλων μας. Στο πέμπτο κεφάλαιο θα μελετήσουμε δεδομένα από την διαστημική αποστολή Kepler της NASA η οποία μας έχει προμηθεύσει με μεγάλο όγκο δεδομένων φωτομετρίας πολύ καλής ακρίβειας και έχει αυτή τη στιγμή ανακαλύψει τον μεγαλύτερο αριθμό έξω-ηλιακών πλανητών με τη μέθοδο των διαβάσεων από οποιοδήποτε άλλο πρόγραμμα που χρησιμοποιεί την ίδια ή οποιαδήποτε άλλη μέθοδο. Αρχικά προσπαθήσαμε να ανιχνεύσουμε φαινόμενα αλληλεπικάλυψης γνωστών πλανητών που πραγματοποιούν διαβάσεις. Τέτοια φαινόμενα υπάρχουν και έχουν ήδη μελετηθεί αλλά όχι εκτενώς. Επιπλέον, ανιχνεύσαμε καμπύλες διαβάσεων που παρουσιάζουν χρονικές διαταραχές και είναι πιθανό να προέρχονται από σύστημα ενός γνωστού και ενός κρυφού πλανήτη.

Στο τελευταίο κεφάλαιο περιγράφεται η προσπάθειά μας να στίσουμε το δικό μας πρόγραμμα επαναληπτικών παρατηρήσεων γνωστών έξω-ηλιακών πλανητών με σκοπό την ανίχνευση χρονικών διαταραχών από τον Αστρονομικό σταθμό Χολομώντα στον Ταξιάρχη Χαλκιδικής. Εκεί, συναρμολογήσαμε τον κατάλληλο εξοπλισμό, και φτιάξαμε μικρά προγράμματα για την οργάνωση των παρατηρήσεων και την επεξεργασία των δεδομένων, φυσικά εκμεταλλευόμενοι τα προγράμματα των πρώτων κεφαλαίων. Δυστυχώς, κάποιες δυσλειτουργίες των οργάνων στην αρχή της χρονιάς και ο κάκιστος ανοιξιάτικος καιρός της περιοχής δεν μας επέτρεψαν να πάρουμε έναν ικανοποιητικό αριθμό παρατηρήσεων. Παρόλα αυτά, υπάρχουν πλέον τα μέσα έτσι ώστε στο μέλλον,μέσω κάποιας άλλης πτυχιακής να συνεχιστεί το έργο που ξεκινήσαμε.

Chapter 1

Introduction to Exo-planets and Exo-planetary Systems

Humanity always tended to question the idea that our civilization is unique in this universe. This concern was, and still is, the driving force of all our efforts to find new planets, planets that may have the same characteristics as the Earth and could host life. In 1930, Pluto, the last planet of our Solar System (today Pluto is considered not to be a planet), was detected and the picture of our Sun's neighbourhood was thought to be completed, without high expectations of finding other forms of life inside its boundaries. Then, astronomers began to think that the existence of other, Sun-like, main-sequence stars hosting other, Earth-like, habitable planets was possible.

1.1 First detections

Van de Kamp (1963) of the Sproul Observatory claimed to have found a planet with 1.6 Jupiter masses on a $4.4 AU$ orbit around a nearby M-dwarf star known as the Barnard's star (named after the discoverer of its very high proper motion) using astrometry. Unfortunately the signal was soon identified as spurious. In subsequent observations, Gatewood and Eichhorn (1973) failed to verify the planetary signal and

Figure 1.1: Astrometry data for Barnard's star published by Van de Kamp (1975).

around the same time Hershey (1973) showed that changes in the astrometric field of various stars were correlated to the timing of adjustments and modifications that had been carried out on the telescopes objective lens. As a result, the planetary discovery was an artefact of maintenance and upgrade work on the telescope and is an excellent example of an uncorrected systematic effect.

Campbell et al. (1988) cautiously claimed to have detected a planet in orbit

around γ Cephei A (γ Cephei is a binary system) using the radial velocity method which we will discuss later. Although, this was the first true planet to be found the confirmation of the discovery came much later by Hatzes et al. (2003) who analysed long-term data and found that the true mass of the planet was $3-16$ Jupiter masses. So this planet is not considered to be the first exo-planet.
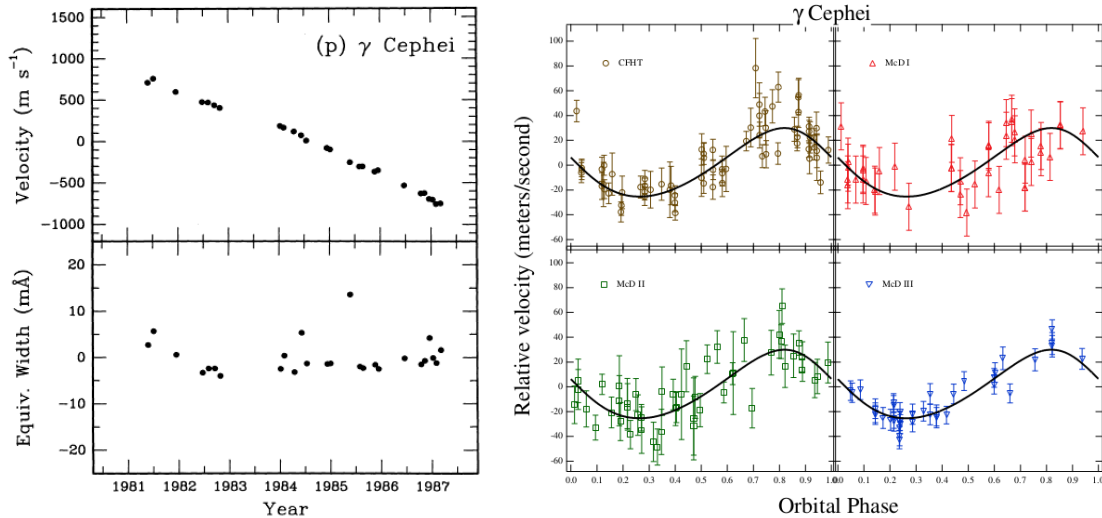
Figure 1.2: Radial velocity data for γ Cephei A published by Campbell et al. (1988) (left) and by Hatzes et al. (2003) (right).
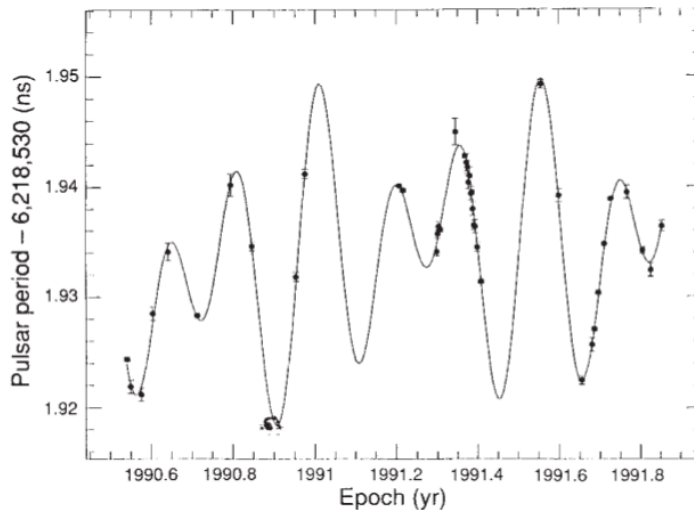
Figure 1.3: Pulsar timing data for PSR B1257+12 published by Wolszczan & Frail (1992).

In the beginning of 90's the $6.2ms$ pulsar PSR B1257+12 was the next celestial object thought to host a planet. Wolszczan & Frail (1992) published their results on the irregularities in the times-of-arrival of the pulsar studied by the giant 305m Arecibo telescope. Their conclusion was that these irregularities must be due to the presence of two planets orbiting the pulsar PSR B1257+12 at $0.47AU$

and $0.36AU$ with masses 2.8 and 3.4 Earth-masses respectively. These was the first exo-planets ever to be found but still the neighborhood of a pulsar could never be a habitable place so the quest for finding other planets orbiting main-sequence stars had just started.

1.2 Exo-planets via spectra

One of the best means that we have to study celestial bodies is spectroscopy. Spectral analysis of the light emitted by a stars not only gives us information about the composition of the star but also about the speed of the star in space and the composition of the matter that surpasses until it reaches the Earth. The first one is possible by using the Doppler effect. When a light source is moving closer to the Earth its light is blue-shifted and when it is moving away from the Earth it is red-shifted. So by observing absorption lines of known elements and chemical compounds we can measure the difference between the observed wavelength λ_o and the wavelength in laboratories λ_s and calculate the parallel to the line of sight speed of the source v in terms of the speed of light c. The relationship is:

$$\frac{\lambda_o - \lambda_s}{\lambda_s} = z = \sqrt{\frac{c+v}{c-v}} - 1 \quad or \quad \frac{\lambda_o - \lambda_s}{\lambda_s} = z = \frac{v}{c} \quad if \quad v \ll c \tag{1.1}$$

1.2.1 Radial velocity or RV

When a planet orbits a star it forces the star to move around the center of their mass on an elliptical orbit of the same eccentricity as its own. As a result the star seems to move some times closer to and some times away from the Earth, a movement that can be detected with spectral analysis and the Doppler effect. The shape of the velocity curve versus time depends on the orbital elements:

$$V_{star} = \frac{2\pi a_1 \sin i}{P\sqrt{1-e^2}} \left[\cos(f+\omega) + e\cos\omega\right] \tag{1.2}$$

where P is the period, i the inclination, ω the argument of periastron and e the eccentricity of the system, a_1 the same-major axis of the stellar orbit and f the true anomaly for each moment.
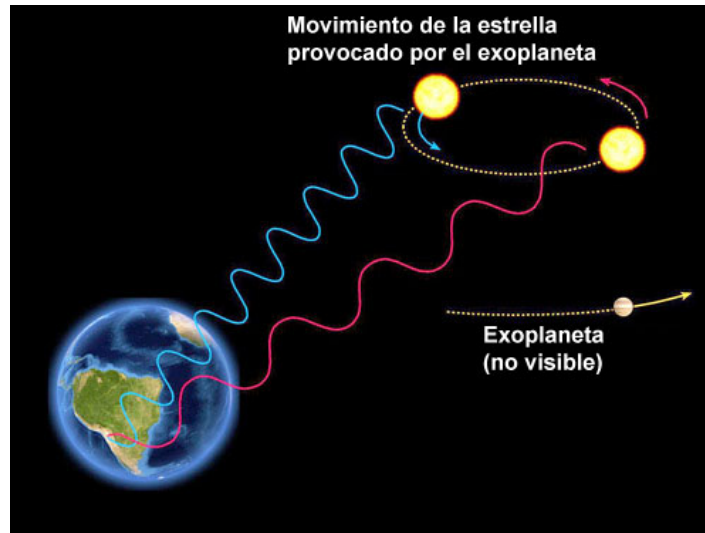

Figure 1.4: Radial velocity variations due to an unseen exo-planet.

The most important result comes from the semi-amplitude of the radial velocity curve, because by findind the period we can use it to find the minimum mass of the planet:

$$K = \left(\frac{2\pi G}{P}\right)^{1/3} \frac{m\sin i}{M^{2/3}} \frac{1}{\sqrt{1-e^2}} \tag{1.3}$$

where m and M the planetary and the stellar mass respectively and G the gravitational constant.

The minimum mass is $m\sin i$ and the true mass m can only be found if the inclination of the orbit is known. If the orbit is too much inclined only a small fraction of the stellar motion can be seen and only a fraction of the planetary mass can be measured.
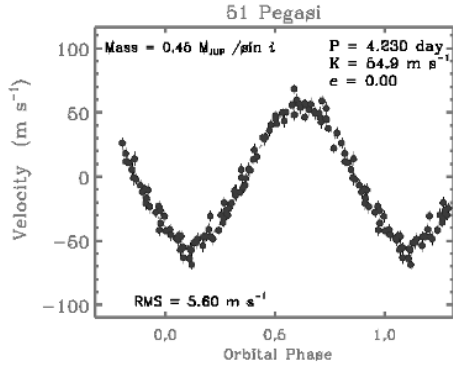
Radial velocity as a detection technique

Figure 1.5: *Radial velocity curve of 51-Peg.*

The analysis of a radial velocity curve from a star-planet system requires high precision spectroscopy and it could not be achieved before the 90's. It was only in 1995 when a radial velocity curve, for the first time, confirmed the existence of an exo-planet. Mayor and Queloz (1995) were looking at 142 bright K and G dwarfs for radial velocity variations. The star 51-Peg is a G-type main sequence star with magnitude of 5.5 located at $15.6pc$ way from the Earth in the Pegasus constellation. The radial velocity curve from this star revealed an exo-planet which existence could not be questioned because the detected signal was strong enough not to allow any doubts. The discovery of the planet orbiting 51-Peg was the big bang of the exo-planetary exploration and practically the beginning of a new era for astronomy, lasting until today. Only six days after the 51-Peg b discovery, Geoff Marcy and Paul Butler of San Francisco State University independently confirmed the signal and also announced two new planets orbiting 70-Vir and 47-UMa.

Radial velocity as a detection technique is efficient mainly in finding high mass, short-period planets known as "hot-Jupiters" because they are too close to its host star and as a result their temperature is very high. Only quite recently, by making use of modern, high resolution spectrometers, RV can can detect planets down to a few Earth-masses, or Super-Earths as the are known but still the challenge of finding Earth-like planets cannot be met.

1.2.2   Rossiter-McLaughlin effect

In the case that the orbital inclination of the planet is close to 90 degrees the planet possibly crosses the projected stellar disc. This phenomenon is called a transit

and we will discuss about it later. Stars usually rotate around a spin axis just like our Sun does (in approximately 27 days) so the one edge seems to approach the Earth and the other to move away from it. As a result of this rotation the absorption spectral lines from the elements and the compounds inside the stellar atmosphere become more wide due to the Doppler effect (photons coming from the approaching side are red-shifted) but their mean wavelength is the same as measured in laboratories.
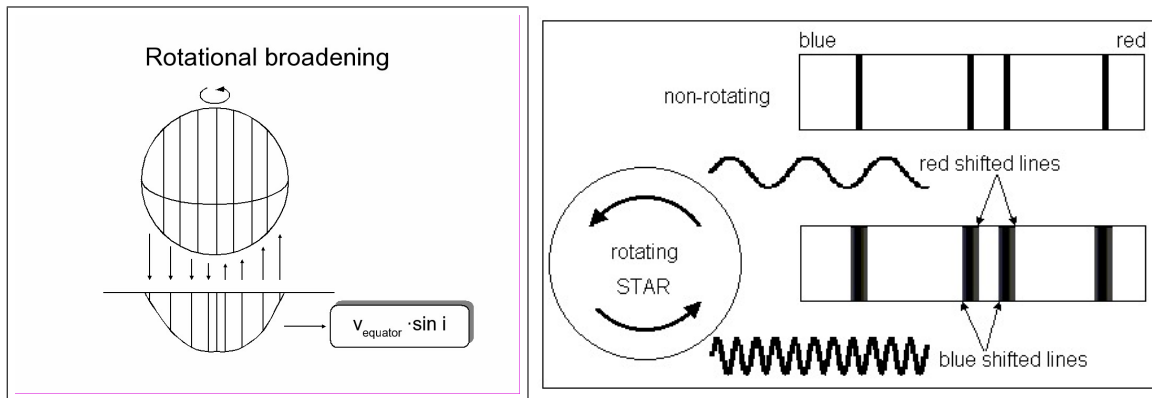
Figure 1.6: Spectral lines broadening due to rotation.

While the planet transits the rotating star it cover a part of it but not constantly the same so some times cover the red-shifted part and others the blue-shifted. As a result the mean value of the wavelength of each spectral line differs from time to time, when the planet cover a blue-shifted part the mean value is red-shifted and vice-versa. The form of the curve depends on the angle between the orbital spin of the planet and the rotational spin of the star λ. If this angle is less that 180 degrees the the red-shifted part will be covered first and the radial velocity will first increase and then decrease but if the angle is larger the blue-shifted part will be covered first and the radial velocity will first decrease and then increase. Until now, all known incidents show that the two spins have the same direction. Moreover, this angle can be measured from the shape of the radial velocity curve, this phenomenon is known as the Rossiter-McLaughlin effect.

Figure 1.7: Radial velocity curves during a transit for different values of λ.

1.2.3   Exo-planetary atmospheres

If an exo-planet is massive enough it can maintain an atmosphere just like the planets in our solar systems. The knowledge of the composition and the structure of such atmospheres is vital if we want one day to find a possibly habitable planet because the atmosphere contains all these elements and compounds that can support or destroy life. There are two cases in which the light that c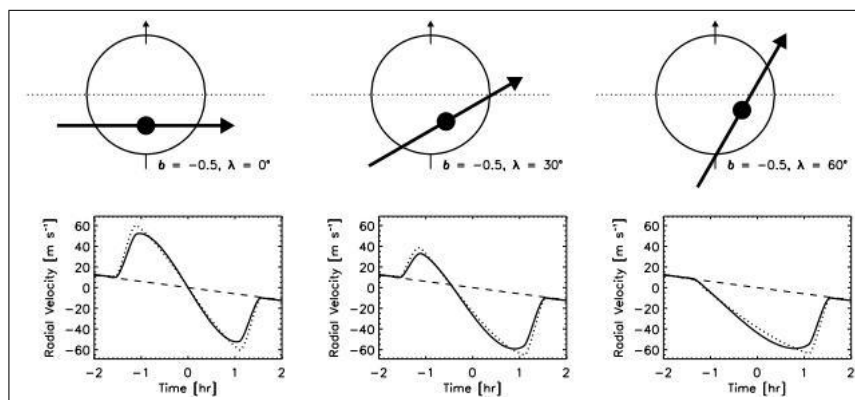ams to our receivers is filtered through an exo-planetary atmosphere and can carry information about (spectral lines) about its compositions and structure.

An exo-planet has a temperature (equilibrium temperature, T_{eq}), because it is heated by its host star, and emits like a black body. If the exo-planet is hot enough its light is detectable in the region of infra-red.

$$T_{eq} = T^*_{eff}(1-a)^{1/4}\sqrt{\frac{R^*}{2d}} \tag{1.4}$$

where T^*_{eff} is the stellar effective temperature, R^* the stellar radius, d the distance between the star and the planet and a the albedo, the percentage of light reflected by the planet back to space.

If the exo-planet transits its host star then at some time it goes behind it an we can measure the difference in infra-red light (secondary eclipse). Deming et al. (2006) measured, with Spitzer's $16\mu m$, the secondary eclipse of HD-189733b with amplitude 40 times the error level. (Swain et al. 2008) announced detection of H_2O and CH_4 in the terminator regions of HD-189733b via near infra-red spectroscopy using the Hubble Space Telescope (HST) and proved that molecular spectroscopy of bright transiting planets is possible. More recently Swain et al. (2009) found water, methane, and carbon dioxide in the atmosphere of HD-209458b.
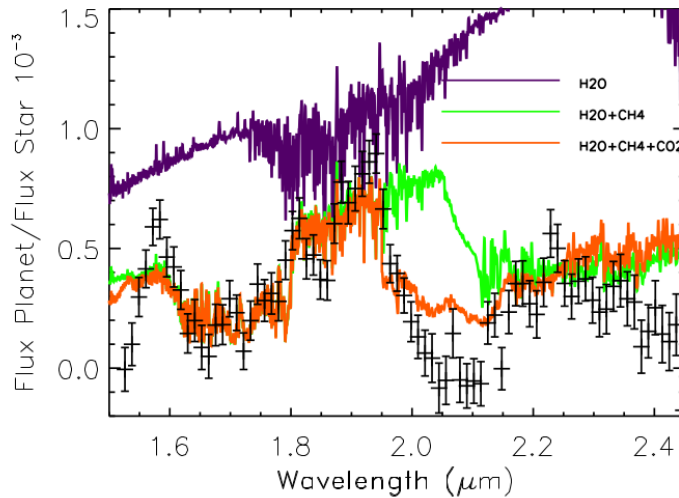

Figure 1.8: Observed and modelled spectrum of HD-189733b from Swain et al. (2009)

EChO (Exoplanet Characterisation Observatory) is a new space-based project proposed by Tinetti et al. (2011) aiming to study the atmospheres of a variety of exo-planets. EChO will provide simultaneous, multi-wavelength spectroscopic

observations with long exposures and will make use of planet transits, secondary eclipses, and planet phase-variations (applied on non-transiting planets too).

1.3 Exo-planets via light-curves

The other significant method for studying celestial bodies is photometry. With photometry we can measure how much light a star emits towards the Earth each moment, we call this stellar property flux and it is the measured in $W/s/m^2$. A star is considered to be a stable source of light and usually flux is constant so we usually use the relative flux, the ratio of stellar flux over its mean flux, to measure any variations in the amount of light that our instruments gather. The curve of relative flux versus time is known as a light-curve. Photometry for exo-planets is being used only during the last two decades because the flux variations due to an exo-planet is too small and high precision is needed, that means very capable equipment something that astronomers did not had before. In the next sections we will discuss about some phenomena that cause variations to the stellar light-curves and are due to the existence of an exo-planet orbiting the star.

1.3.1 Micro-lensing

Stars are seen to be stable on the celestial sphere but in fact they have proper motions and their positions change with time and stars closer to the Earth seem to move faster. Consider such a star to move on the celestial sphere and some time, accidentally, passes between the Earth and an other star more distant. Today we know from the theory of relativity that massive bodies distort the time-space around them

Figure 1.9: Gravitational lens.

and bend the apparent path of light that passes close to them just like a lens. This effect is called gravitational lensing and in our case the closer star is a lens which cause the flux of the more distant star to increase significantly for a few days or weeks. In the case that the closer planet hosts a planet it may also passes in front of the star and cause a second, smaller, increase.

Micro-lensing as a detection technique

For stellar masses, the field of view of the gravitational lens is tiny (1mas) so the probability of seeing another star within its field of view is extremely small, typically of order 10^{-6}. While it is quite impractical to monitor any single lens in the hope of seeing a star pass through it, there are several well-established and efficient surveys specifically designed to detect gravitational micro-lensing events. This is achieved

by surveying regions in the galactic bulge where star densities are very high and measuring the brightness of roughly one hundred million stars each night.

There are two important micro-lensing surveys are the Optical Gravitational Lensing Experiment (OGLE) at Las Campanas Observatory in Chile and the Microlensing Observations in Astrophysics (MOA) at Mt. John Observatory in New Zealand. Micro-lensing is a detection method that gave results for the first when Bond et al. (2004) published the discovery of OGLE 2003-BLG-235/MOA 2003-BLG-53, (it was found and named by both survey projects) a planet with 1.5 Jupiter masses at a distance of $3AU$ from its hosting star.
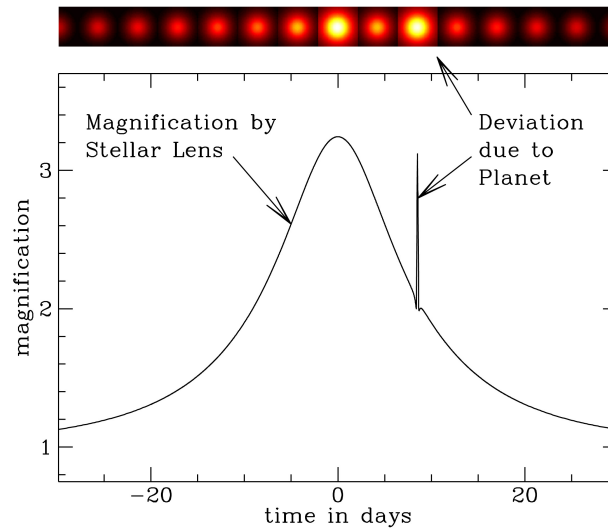
Figure 1.10: Gravitational micro-lensing due to an exo-planet.

Although, this method has given some results until today with more on-going projects, it can only be used to detect massive planets quit far away from their hosting stars making it impossible to host life. An other disadvantage is that the phenomenon takes place only once and follow up observations cannot be done.
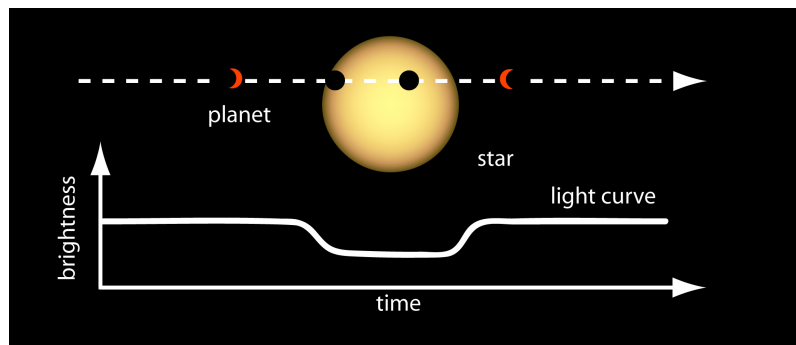
1.3.2 Transit

Figure 1.11: A very simple illustration of a transit.

A transit is the observed drop in the light-curve of a star when a planet that orbits it passes in front of it and blocks a part of its light. The transit phenomenon gives as a tremendous amount of information about the orbit of the planet its size, composition, oblateness, atmosphere (as discussed above), temperature, albedo and habitability in general. Planets that cause transits are referred to as transiting planets. A detailed analytical function for a transit does not exists due to the complexity of the phenomenon (see chapter 3).

An important result comes from the depth of the light-curve, because it is related to the star-planet radii ratio:

$$\delta = \frac{R_{planet}^2}{R_{star}^2} \tag{1.5}$$

Transit as a detection technique

Charbonneau et al. (2000) and Henry et al. (2000) detected the first transit of an extrasolar planet for HD 209458b, a fairly typical hot-Jupiter around a bright star. Since then the surveys for transiting planets increased rapidly and soon the first space-base projects were designed and launched. These are mainly two, Corot from ESA and Kepler from NASA. About the kepler mission we will talk extensively in chapter 5.

1.4 The exo-planetary map today

Until now (2nd of July, 2014) the different detection methods (micro-lensing, RVs, transits, direct imagining etc.) have found 1737 confirmed exo-planets in 451 exo-planetary systems and there are also an other 4234 candidates (source: NASA EXOPLANET ARCHIVE). One of the most popular and interesting diagrams is that of planetary mass with orbital period.
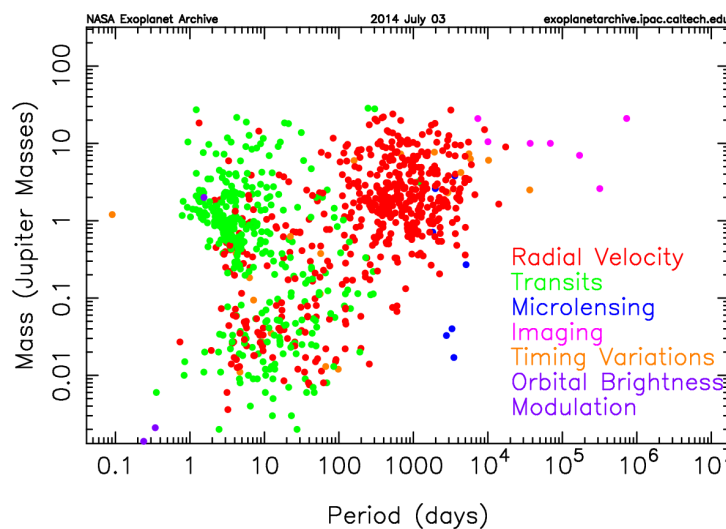

Figure 1.12: Planetary mass - orbital period diagram for the different detection methods.

1.5   Light-curves from exo-planetary systems

In the previous sections we discussed about the distortions that an exo-planet can cause to the rv-curve and the light-curve of its host star. What happens if we add an additional planet in the same system? The phenomena caused by the first planet are distorted too, so we are talking about second degree distortions. We will refer to two kinds of such distortions in a light-curve, and more specifically in a transit light-curve. Very early in the modern exo-planetary history, when the number of planets begun to increase rapidly and the space missions where being prepared, astronomers proposed that the planets were to be discovered would not be alone.

1.5.1   Multi-transiting systems and the overlapping double transit

Planets detected by transits are the most well described because, as we will see in the next chapter, the transit light-curve depends on almost all the orbital parameters of the planet. Consider, now, a planetary system with more than one transiting planets. In this case the information collected are enough to characterise the structure of the system. As our knowledge about the structure of exo-planetary systems increases we will be able to study in more detail the formation of planetary systems, including our own.

The Kepler Space Telescope (Borucki et al. 2010) has until now revealed many multi-transiting systems, most of them very recently (Lissauer et al. 2014; Rowe et al. 2014)
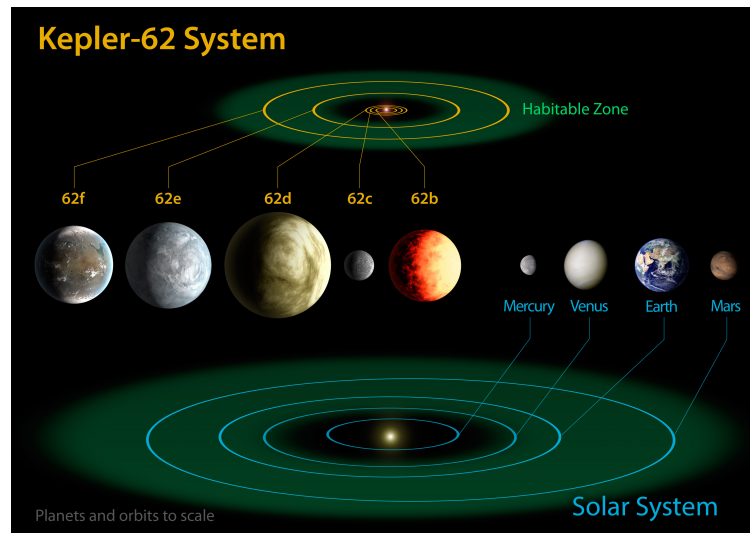
Figure 1.13: Kepler-62 system compared with our solar system.

In such systems we have a unique opportunity to observe mutual events and the one that we will discuss is the transit of an outer planet over an inner, while they are simultaneously transiting their host star. Following the terminology of Ragozzine & Holman (2010) we will call this phenomenon the overlapping double transit. Such an event is very important because it is very powerful in determining the orbital parameters of the two planets, as they are in precise projected positions at a precise moment. In this thesis we will use a new numerical model to simulate

the exact stellar flux-drop during a planet-planet eclipse towards the calculation of
the mutual inclination of the two overlapping planets. Mutual inclination is a very
important orbital element for a system because it is related to its formation and
structure.
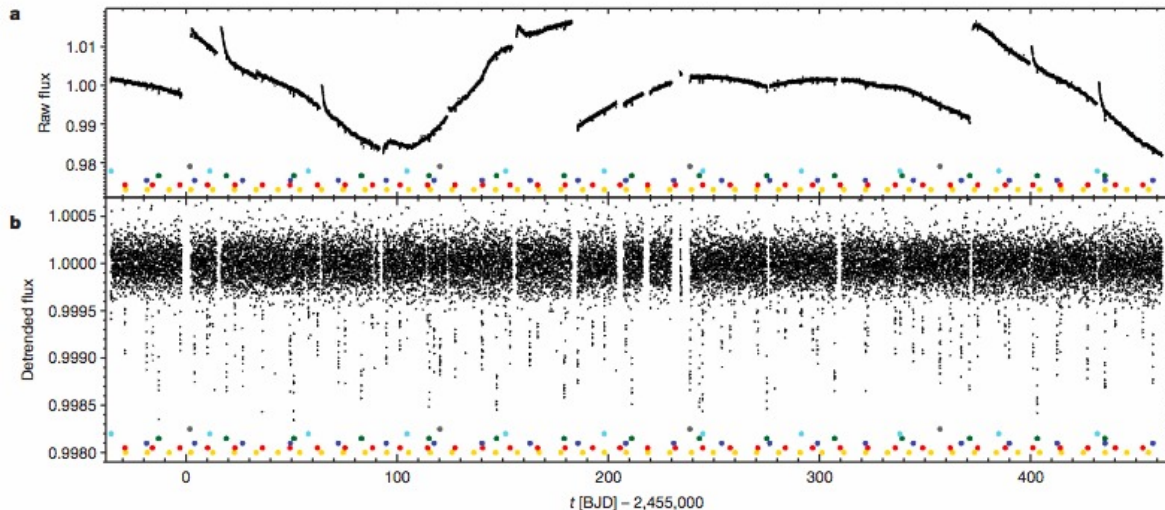
*Figure 1.14: Kepler-11 system. The differently coloured dots indicate the transit of each
different planet.*

1.5.2   Transit timing variations or TTVs

Transiting planets cause a flux-drop to the stellar light once per a complete orbit
with the time intervals between each transit expected to be exactly equal to the
period. Measuring variations of the timing of transits it is possible to reveal the
existence of an additional planet, not necessarily transiting, some times with mass
comparable to one Earth-mass (Holman & Murray 2004). In such a case, the grav-
itational perturbations of the additional planet on the orbit of the transiting planet
forces the transit to happen earlier or later, this distortion is called transit timing
variations or TTVs.

Agol et al. (2004) computed the magnitude of these variations for some theo-
retical exo-planetary systems and came to very interesting conclusions (table 1.1).
According to them, an earth mass planet in 2:1 resonance with a 3-day period tran-
siting planet (e.g. HD 209458b) would cause timing variations of order 3 minutes,
which would be accumulated over a year and easily detectable.

The most recognisable eco-planet with TTVs is KOI-142b which was recently
confirmed to have an additional, non-transiting, planetary companion. KOI-142b is
a transiting exo-planet, found by the Kepler mission, with period of 10.95 days and
TTVs of more that 10 hours. These TTVs were first pointed out by Ford et al. (2011,
2012) and Steffen et al. (2012) and updated by Mazeh et al. (2012). Nesvorny et
al. (2013) used them to detect an additional, non-transiting, planetary companion
(KOI-142c) with mass $\simeq$ 0.7 Jupiter masses close to a 2:1 resonance with KOI-
142c. Finally, Barros et al. (2014) confirmed the existence of the companion via
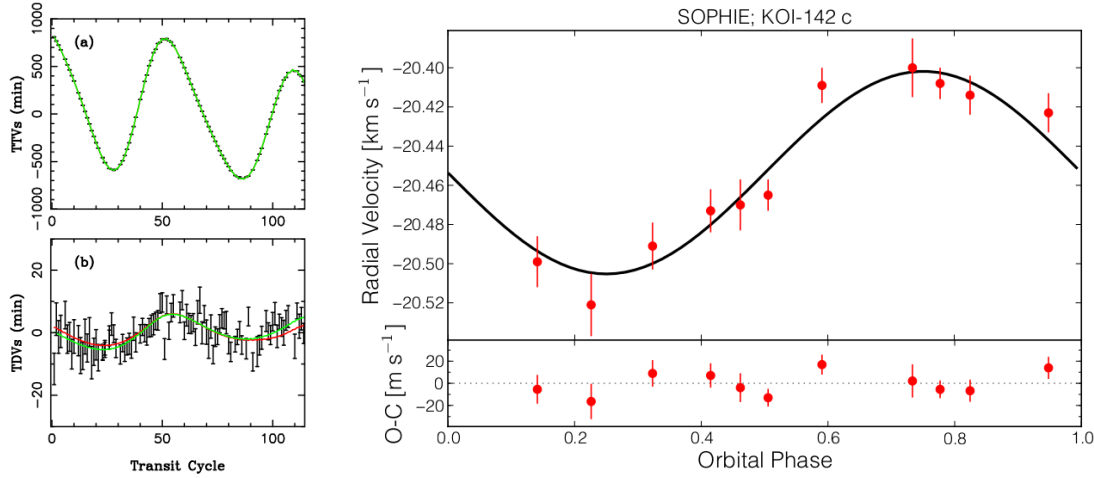radial velocity measurements.

Figure 1.15: KOI-142 TTVs and TDVs (Transit Duration Variations) from Nesvorny et al. (2013) (left) and radial velocity measurements from Barros et al. (2014) (right).

Table 1.1: Cases and conclusions of Agol et al. (2004)

case	conclusion
interior perturbing planets with much smaller periods	Planet-planet perturbations are negligible. The main effect is the wobble of the star due to the inner planet, therefore $\delta t \sim \mu_{in}(a_{in}/a_{out})P_{out}$.
exterior perturbing planets on eccentric orbits with much larger periods	The exterior planet changes the period of the interior one by $\mu_{out}(a_{in}/a_{out})^3 P_{in}$. As the distance of the exterior planet changes due to its eccentricity, the inner planets period changes. Deviations in its transit timing accumulates over the period of the outer planet, therefore $\delta t \sim \mu_{out}e_{out}(a_{in}/a_{out})^3 P_{out}$.
both planets on circular orbits with arbitrary period ratio but not in resonance	Half way between resonances the perturbations are small, of order $\mu_{out}a_{in}^2/(a_{in}-a_{out})^2 P_{in}$ for the inner planet (switch out and in for the outer planet). This increases as one gets closer to a resonance.
planets on initially circular orbits locked in resonance	In resonances the perturbations are the largest. As long as the perturber is more massive than the transiting planet, the timing variations would be of order of the period regardless of the perturber mass.
Notes	Subscripts "out" and "in" refer to the exterior and interior planets and μ is the planet to star mass ratio.

From the above we can understand the significance of TTVs for the quest of extra-solar planets and planetary systems detection and study. In this thesis we will try to search for TTVs in the light-curves of Kepler Objects of Interest (KOIs) and also to set up our own follow-up program for TTVs analysis and possible detection of additional non-transiting planets from the Holomon Astronomical Station of the Aristotle University of Thessaloniki. Although we would like to built a code for TTVs analysis through numerical integration of the tree-body problem this was beyond the limits, mainly time limit, of this diploma thesis and so we will try it in the future.

Chapter 2

The Transit Light-curve

If we want to study the transit of an exo-planet and, afterwards, the perturbations caused on it from an additional exo-planet in the same system we have to be able to reproduce a transit light-curve and contrast it with real data. In this chapter we will describe how this can de achieved by calculating the projected distance, or separation, between the host star and the planet and the flux drop that the planet causes to the stellar light. We also developed a simple software to serve this purpose and use it in the future.

2.1 The projected distance function

In the case of a planet orbiting a star the calculation of their projected distance on the celestial sphere is not so complicated because the solution of the two body problem is known.

2.1.1 Planetary orbit

Such a motion occurs on a single orbital plane and both the apparent and the relative orbits are ellipses with the same eccentricity (figure 2.1).
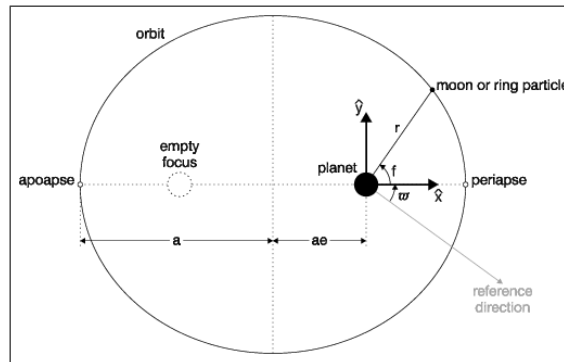
$$r(t) = \frac{a(1 - e^2)}{1 + e \cos f(t)} \tag{2.1}$$

Figure 2.1: Planetary orbit.

where a is the semi-major axis and e the eccentricity of the ellipse and f which is called *true anomaly* and it is the angle between the line joining the star and the planet each moment and the line joining the star and the periastron, the orbital point closest to the star.

The geometrical parameters of the eclipse (a and e) are connected to the energy and the angular momentum of the system.

$$a = -\frac{k}{2E}$$
$$e = \sqrt{1 + \frac{2EL^2}{k^2}} \tag{2.2}$$
$$k = G(M + m)$$

where E and L are the energy and the angular momentum of the system per unit of mass respectively, M and m are the stellar and the planetary masses respectively and G is the gravitational constant.

2.1.2 Planetary orbit as seen from the Earth

When this ellipse is observed from the Earth we need three additional angles to characterize the orientation of the ellipse in space.
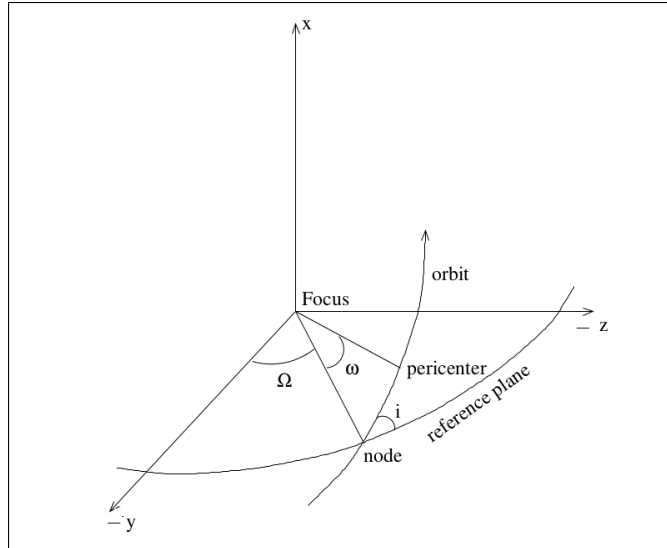
Figure 2.2: The planetary orbit as seen from the Earth.

Assume that we have a Cartesian coordinate system with the star at the beginning of axes and the Earth at position $(+\infty, 0, 0)$. The plane of reference, the plane perpendicular to the line of sight is (yz). The first angle that we need is the *inclination*, i, of the orbital plane with respect to the reference plane (yz).

If inclination is not zero then the orbit intersects the reference plane (yz) in two points, the ascending and the descending node. The nodes are the points where the planet and the star lay both on the reference plane (yz) but when the planet passes the ascending node it comes closer to the Earth than the star and when it passes the descending node it goes further from the Earth than the star. The other angle

that we need is the angle between the line connecting the beginning of axes and the ascending node and the y axis. This angle is called the *longitude of the node* and denoted by Ω.

The third and final angle is the one that gives us the orientation of the ellipse on the orbital plane with respect to our Cartesian system. It is the angle between the line connecting the beginning of axes and the periastron and the line connecting the beginning of axes and the ascending node. This angle is measured on the orbital plane, it is called the *argument of periastron* and denoted by ω.

2.1.3 Projected distance as function of true anomaly

Having defined the orbital elements, lets calculate now the projected distance of the star and the planet. To achieve this we have to express the position of the planet (x,y,z) in terms of the orbital elements. Consider the previous Cartesian coordinate system with the star at the beginning of axes and the Earth at position $(+\infty, 0, 0)$. For $i = 0$, $\omega = 0$, $\Omega = 0$ assume that the major axis of the ellipse is on the y axis and for the periastron $y < 0$. In this case we will have:

$$x_1(t) = 0$$
$$y_1(t) = -r(t)\cos f(t) = -\frac{a(1 - e^2)}{1 + e\cos f(t)}\cos f(t)$$
$$z_1(t) = -r(t)\sin f(t) = -\frac{a(1 - e^2)}{1 + e\cos f(t)}\sin f(t)$$

(2.3)

If we rotate the ellipse by an angle ω with respect to the negative y axis we will have:

$$x_2(t) = 0$$
$$y_2(t) = y_1(t)\cos\omega - z_1(t)\sin\omega = -\frac{a(1 - e^2)}{1 + e\cos f(t)}\cos(f(t) + \omega)$$
$$z_2(t) = y_1(t)\sin\omega + z_1(t)\cos\omega = -\frac{a(1 - e^2)}{1 + e\cos f(t)}\sin(f(t) + \omega)$$

(2.4)

Lets now incline the orbital plane with respect to the y axis by an angle i:

$$x_3(t) = -z_2(t)\sin i = \frac{a(1 - e^2)}{1 + e\cos f(t)}\sin(f(t) + \omega)\sin i$$
$$y_3(t) = y_2(t) = -\frac{a(1 - e^2)}{1 + e\cos f(t)}\cos(f(t) + \omega)$$
$$z_3(t) = z_2(t)\cos i = -\frac{a(1 - e^2)}{1 + e\cos f(t)}\sin(f(t) + \omega)\cos i$$

(2.5)

Finally, we have to rotate the projected ellipse by an angle Ω to the positive direction:

$$x_4(t) = x_3(t) = \frac{a(1 - e^2)}{1 + e \cos f(t)} \sin(f(t) + \omega) \sin i$$

$$y_4(t) = y_3(t) \cos \Omega - z_3(t) \sin \Omega = \frac{a(1 - e^2)}{1 + e \cos f(t)} \left[-\cos(f(t) + \omega) \cos \Omega + \sin(f(t) + \omega) \sin \Omega \cos i \right]$$

$$z_4(t) = y_3(t) \sin \Omega + z_3(t) \cos \Omega = \frac{a(1 - e^2)}{1 + e \cos f(t)} \left[-\cos(f(t) + \omega) \sin \Omega - \sin(f(t) + \omega) \cos \Omega \cos i \right]$$

$$(2.6)$$

The projected distance between the star and the planet will, finally, be:

$$z(t) = \sqrt{y_4(t)^2 + z_4(t)^2} = \frac{a(1 - e^2)}{1 + e \cos f(t)} \sqrt{\cos^2(f(t) + \omega) + \sin^2(f(t) + \omega) \cos^2 i} \qquad (2.7)$$

2.1.4   Projected distance as function of time

Equations 2.6 return the position of the planet as a function of true anomaly but for us it is more convenient to have the position of the planet as a function of time. Unfortunately there is no analytic relation between true anomaly and time.

For this reason an other angle is introduced, the *eccentric anomaly*, E, which is shown in figure 2.3. This angle has a relation with both true anomaly and time, so it is used to change time into true anomaly. The relation between the eccentric anomaly and time is known as the *Kepler equation*.
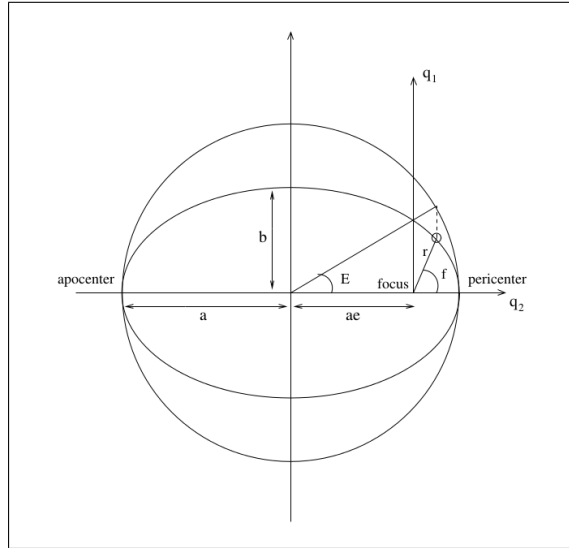

Figure 2.3: True and eccentric anomaly.

$$E(t) - e \sin E(t) = \frac{2\pi}{P}(t - t_0) \qquad (2.8)$$

$$E(t) = 2 \tan^{-1} \left[\sqrt{\frac{1 - e}{1 + e}} \tan \left(\frac{f(t)}{2} \right) \right] \qquad (2.9)$$

$$f(t) = 2\tan^{-1}\left[\sqrt{\frac{1+e}{1-e}}\tan\left(\frac{E(t)}{2}\right)\right] \qquad (2.10)$$

where E is the eccentric anomaly, f the true anomaly, e the orbital eccentricity, P the orbital period and t_0 the time of periastron, the moment that the planet passed once from the periastron.

For transiting planets, P can be calculated from the time separation between transits and t_0 from the mid-transit point, t_{mtp}, of the first observed transit.

At t_{mtp}, the star, the planet and the Earth are aligned, so for $f(t_{mtp})$ we have:

$$f(t_{mtp}) = \begin{cases} \pi/2 - \omega & \text{if } \omega \leq \pi/2 \\ 5\pi/2 - \omega & \text{if } \omega > \pi/2 \end{cases} \qquad (2.11)$$

Using equation 2.9 we calculate $E(t_{mtp})$ and then using equation 2.8, t_0:

$$E(t_{mtp}) = 2\tan^{-1}\left[\sqrt{\frac{1-e}{1+e}}\tan\left(\frac{f(t_{mtp})}{2}\right)\right] \qquad (2.12)$$

$$t_0 = t_{mtp} - \frac{P}{2\pi}\left(E(t_{mtp}) - e\sin E(t_{mtp})\right) \qquad (2.13)$$

Finally, for each t_i we can find $E(t_i)$ by solving numerically equation 2.8, $f(t_i)$ from equation 2.10 and therefore the position of the planet from equations 2.6.

$$E(t_i) - e\sin E(t_i) = \frac{2\pi}{P}(t_i - t_0) \qquad (2.14)$$

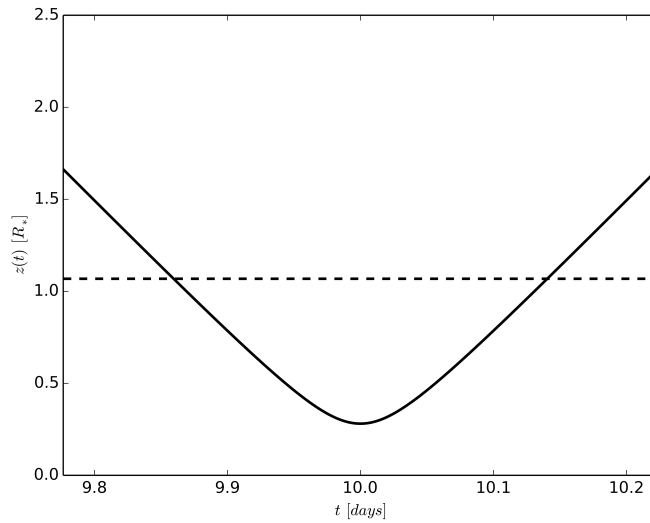$$f(t_i) = 2\tan^{-1}\left[\sqrt{\frac{1+e}{1-e}}\tan\left(\frac{E(t_i)}{2}\right)\right] \qquad (2.15)$$

Figure 2.4: Projected distance between a planet and its host star as function of time for $P = 22.343days$, $a = 26.099R_*$, $e = 0$, $i = 89.383^o$, $\omega = 0^o$, $\Omega = 1.04^o$, $t_{mtp} = 10days$ and $p = 0.069R_*$. The dashed line is the transit limit $1 + p$.

2.2 The flux-drop function

The next step in order to reproduce a transit light-curve is the calculation of the exact flux-drop that the planet causes to the host star. To do so, we assume a polar coordinate system in witch the star is a positive flux circle area with $R = 1$, centred at $(0, 0)$ and the planet is a zero flux circle area with $R = p$, centred at $(z, 0)$. All the lengths are normalized over the stellar radius.
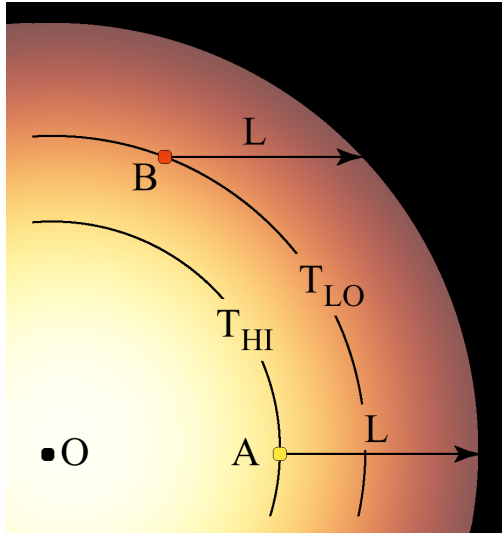
2.2.1 Limb darkening

Figure 2.5: The limb-darkening mechanism.

Limb darkening is an optical effect and it is the result of thermodynamics and optics. According to that, the flux of a star is not constant throughout the hole projected disk but it is a function of the projected distance from the center $(0, 0)$.

When we look at a specific point of the stellar surface, the light what we see comes from a depth which has an optical depth of a untie. So as we look closer to the limb this depth decreases (in figure 2.5 point A is closer to the center of the star than point B). But, as we know, the closer to the center of the star the higher the temperature. As a result, according to the Stefan-Boltzmann law for a Black Body radiation, the points closer to the center of the stellar disk seem to emit more energy and the observed flux is higher.

In order to be accurate, our calculation of the flux-drop during a transit has to take into account the limb-darkening phenomenon. Some proposed functions are:

Linear law:

$$I(\mu) = 1 - u(1 - \mu) \tag{2.16}$$

Quadratic law:

$$I(\mu) = 1 - a(1 - \mu) - b(1 - \mu)^2 \tag{2.17}$$

Square root law:

$$I(\mu) = 1 - c(1 - \mu) - d(1 - \sqrt{\mu}) \tag{2.18}$$

Logarithmic law:

$$I(\mu) = 1 - e(1 - \mu) - f\mu \ln \mu \tag{2.19}$$

Exponential law:

$$I(\mu) = 1 - g(1 - \mu) - h\frac{1}{1 - e^\mu} \tag{2.20}$$

Four elements law (Claret 2000):

$$I(\mu) = 1 - a_1(1 - \mu^{1/2}) - a_2(1 - \mu) - a_3(1 - \mu^{3/2}) - a_4(1 - \mu^2) \qquad (2.21)$$

In the previous equations 2.16-2.21 it is assumed that $I = 1$ at the center $(0, 0)$. Moreover, $\mu = \cos(\gamma)$ where γ is the angle between the line of sight and the emergent intensity. As seen in figure 2.6 for μ we have:

$$\mu = \cos(\gamma) = \frac{d}{1} = \sqrt{1 - r^2} \qquad (2.22)$$
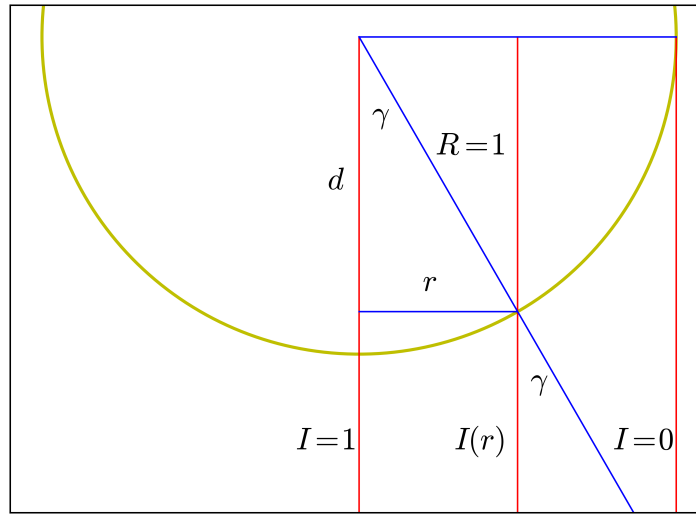
Figure 2.6: I(r) geometry.

For our calculations we will use equation 2.21. Notice that for $r = 1$, $I(r) \neq 0$, this is a problem of the limb-darkening coefficients. This coefficients are different for each star depending on the stellar parameters such as the effective temperature the gravitational acceleration and the metallicity and were derived from the study of many different stars (Claret et al. 2004). Claret et al. used a least square method and as a result the coefficients they give correctly simulating the stellar intensity but they are not fixed to give $I(r) = 0$ for $r = 1$.

Figure 2.7: $I(r)$ according to equation 2.21 for $a_1 = 0.4217$, $a_2 = 0.5705$, $a_3 = -0.3582$, $a_4 = 0.0820$.

2.2.2 Calculation

The result will be given by the integrate:

$$\Delta F(z(t)) = \frac{1}{F_0} \int_{u1}^{u2} \int_{r1}^{r2} I(r) r \, dr \, du \Rightarrow \Delta F(z(t)) = \frac{1}{F_0} \int_{u1}^{u2} A(r_2) du - \frac{1}{F_0} \int_{u1}^{u2} A(r_1) du$$

$$(2.23)$$

where, by using equation 2.21 we have:

$$A(r) = \frac{1}{2}(1 - a_1 - a_2 - a_3)r^2 - \frac{1}{4}a_4 r^4 - \frac{2}{5}a_1(1 - r^2)^{5/4} - \frac{2}{6}a_2(1 - r^2)^{6/4} - \frac{2}{7}a_3(1 - r^2)^{7/4}$$

$$F_0 = \int_0^{2\pi} \int_0^1 I(r) r \, dr \, du = 2\pi \left[A(1) - A(0) \right] = 2\pi \left(\frac{1}{2} - \frac{1}{10}a_1 - \frac{1}{6}a_2 - \frac{3}{14}a_3 - \frac{1}{4}a_4 \right)$$
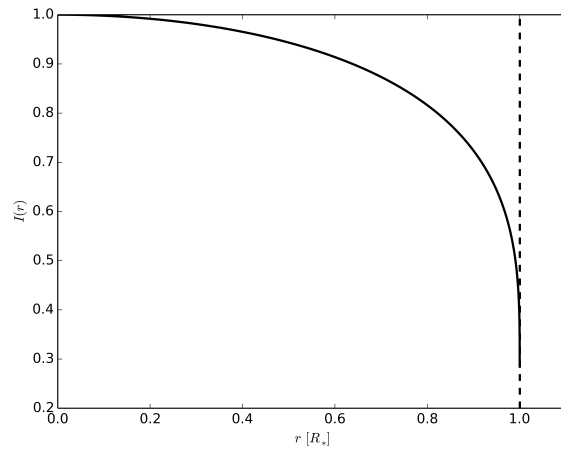
The integration limits are given by the the planet circle in polar coordinates. This integration is quite complicated and the way of calculation is related to the star-planet separation $z(t)$. There are 6 different main cases of star-planet separation (with $p < 0.5$) which have to be treated differently. These cases can be seen in the next figure (2.2).

In table 2.1 you can see all the six cases and the integration limits for each of them, for $z(t) \geq 1 + p$ there is no flux-drop. Notice that in most of the cases one part of the $A(r)$ function has to be solved numerically.

Table 2.1: Star-planet separation cases for $p < 0.5$.

Case	condition
A	$z = 0$
B	$0 < z < p$
C	$z = p$
D	$p < z \leq 1 - p$
E	$1 - p < z \leq \sqrt{1 - p^2}$
F	$\sqrt{1 - p^2} < z < 1 + p$

Table 2.2: Integration limits for the six cases, where $\phi = \sin^{-1}\left(\frac{p}{z}\right), \quad \theta = \cos^{-1}\left(\frac{1 - p^2 + z^2}{2z}\right)$.

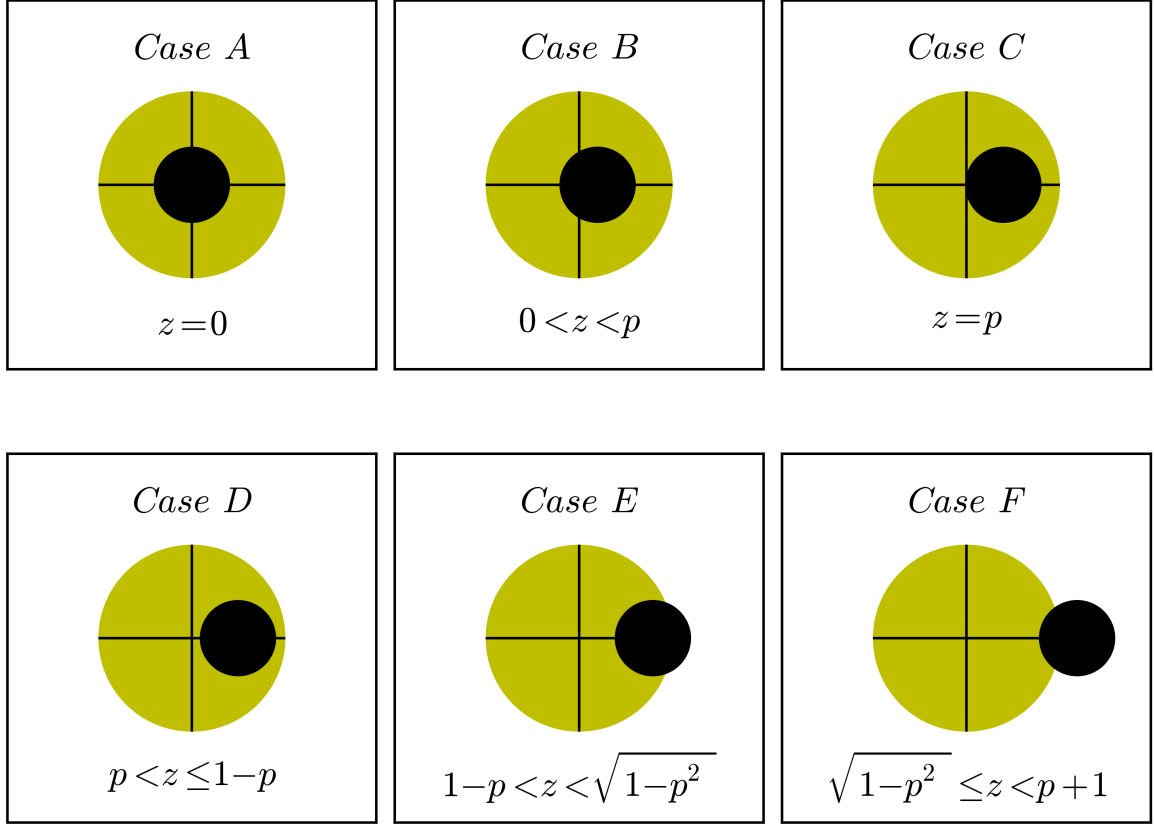| Case	u_1	u_2	r_1	r_2	
A	0	π	0	p	(×2)
B	0	π	0	$z\cos u + \sqrt{p^2 - (z\sin u)^2}$	(×2)
C	0	$\frac{\pi}{2}$	0	$z\cos u + \sqrt{p^2 - (z\sin u)^2}$	(×2)
D	0	ϕ	$z\cos u - \sqrt{p^2 - (z\sin u)^2}$	$z\cos u + \sqrt{p^2 - (z\sin u)^2}$	(×2)
E_1	0	θ	$z\cos u - \sqrt{p^2 - (z\sin u)^2}$	1	(×2)
E_2	θ	ϕ	$z\cos u - \sqrt{p^2 - (z\sin u)^2}$	$z\cos u + \sqrt{p^2 - (z\sin u)^2}$	(×2)
F	0	θ	$z\cos u - \sqrt{p^2 - (z\sin u)^2}$	1	(×2)

Figure 2.8: Star-planet separation cases for $p < 0.5$.
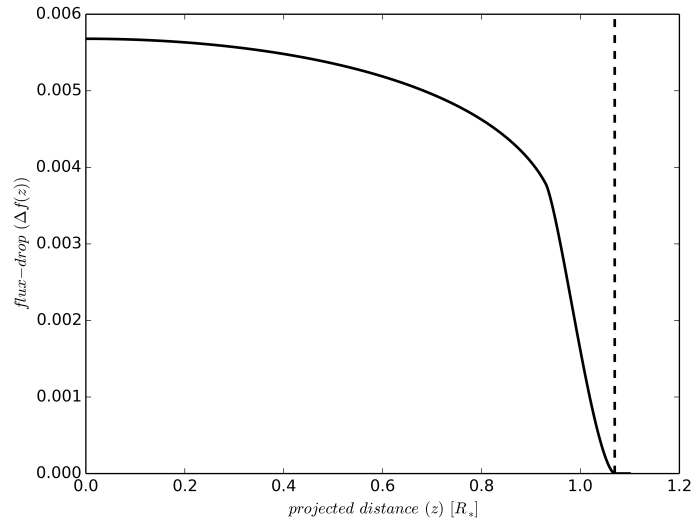

Figure 2.9: $\Delta F(z(t))$ according to equation 2.21 for $a_1 = 0.4217$, $a_2 = 0.5705$, $a_3 = -0.3582$, $a_4 = 0.0820$ and $p = 0.069$. The dashed line is the transit limit $1 + p$.

2.2.3   Pal's flux-drop function.

A very powerful and fast way to calculate a transit model is using the quadratic limb darkening law because there is an analytic expression for that (Pal 2008):

$$\Delta f = W_0 F_0 + W_2 F_2 + W_1 \left[F_1 + F_K K(k) + F_E E(k) + F_\Pi \Pi(n, k) \right] \tag{2.24}$$

Where $K(k), E(k), \Pi(n, k)$ are the complete elliptic integrals of the first, second and third kind, respectively. These and the other functions F are calculated for twelve different cases depending on the projected distance between the host star and the planet. All the details of the calculation can be found in his paper.

2.3   The transit light-curve

Summarising the previous sections, in order to reproduce the transit light-curve we have to follow the next steps:

- Input the orbital elements P, a, e, i, ω and Ω, the mid-transit point t_{mtp} and the different t_i moments for which we want to simulate the light-curve.

- Input the planetary radius p, and the limb-darkening coefficients a_1, a_2, a_3, a_4.

- Calculate the time of periastron t_0 using equations 2.11, 2.12 and 2.13.

- Calculate $f(t_i)$ for each moment using the equations 2.14 and 2.15.

- Calculate the projected distance between the star and the planet $z(t_i)$ for each moment using equation 2.7.

- Calculate the integrate 2.23 $\Delta F(z(t_i))$ for each moment if $x_4(t_i)$ in equations 2.6 is positive.
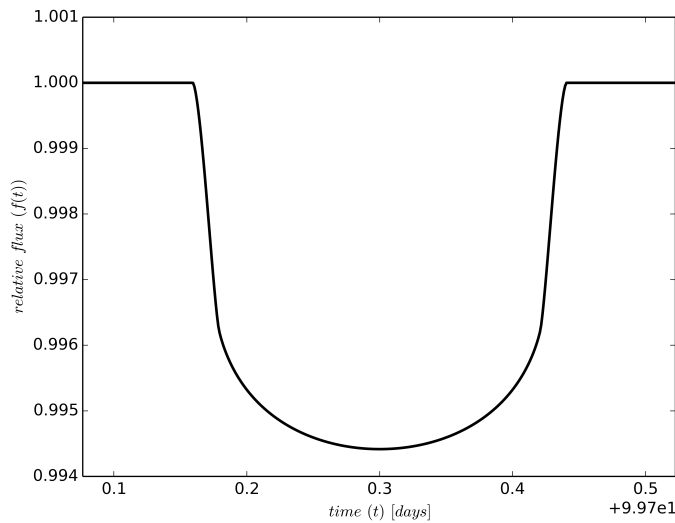

Figure 2.10: The transit model for $a_1 = 0.4217$, $a_2 = 0.5705$, $a_3 = -0.3582$, $a_4 = 0.0820$, $p = 0.069[R_*]$, $P = 22.343 days$, $a = 26.099 R_*$, $e = 0$, $i = 89.383^o$, $\omega = 0^o$, $\Omega = 1.04^o$, $t_{mtp} = 10 days$

Chapter 3

The Overlapping Transit Light-curve

In the case of two transiting planets in an exo-planetary system there is the possibility of alignment between the two planets during their transits. So, for an observer from the Earth, the two planets and the host star will be on his line of sight. As a result the transit light-curve of the outer planet will appear to be distorted because for a few moments the outer planet will not cover only a part of the stellar disk but also a part of the disk of the inner planet. The distortion will have the form of a small jump and in the following paragraphs we will try to calculate the magnitude of this jump and reproduce the light-curve of this phenomenon which is called the overlapping double transit or planet-planet eclipse.

3.1   Positions of the two planets

In order to reproduce the overlapping double transit light-curve we have to find the projected distances between each planet and the host star and the projected distance between the two planets as functions of time.

We assume again keplerian orbits for the two planetary companions and we do not take into account the orbital perturbations that each planet causes to the other. So, the coordinates of each planet, in the same Cartesian system that we used in the previous chapter, will be:

$$
\begin{aligned}
\bar{x}_j(t) =& \frac{a_j(1-e_j^2)}{1+e_j\cos f_j(t)}\sin(f_j(t)+\omega_j)\sin i_j \\
\bar{y}_j(t) =& \frac{a_j(1-e_j^2)}{1+e_j\cos f_j(t)}\left[-\cos(f_j(t)+\omega_j)\cos\Omega_j + \sin(f_j(t)+\omega_j)\sin\Omega_j\cos i_j\right] \qquad (3.1) \\
\bar{z}_j(t) =& \frac{a_j(1-e_j^2)}{1+e_j\cos f_j(t)}\left[-\cos(f_j(t)+\omega_j)\sin\Omega_j - \sin(f_j(t)+\omega_j)\cos\Omega_j\cos i_j\right]
\end{aligned}
$$

Using them, we can calculate the projected distances between each planet and the host star:

23

$$z_j(t) = \sqrt{\bar{y}_j(t)^2 + \bar{z}_j(t)^2} = R_j\sqrt{A_j^2 + B_j^2} \quad \text{where} \quad j = 1, 2 \qquad (3.2)$$

and the projected distance between the two planets:

$$z_{12}(t) = \sqrt{(\bar{y}_1(t) - \bar{y}_2(t))^2 + (\bar{z}_1(t) - \bar{z}_2(t))^2} \Rightarrow$$

$$z_{12}(t) = \sqrt{\bar{y}_1(t)^2 + \bar{z}_1(t)^2 + \bar{y}_1(t)^2 + \bar{z}_1(t)^2 - 2(\bar{y}_1(t)\bar{y}_2(t) + \bar{z}_1(t)\bar{z}_2(t))} \Rightarrow$$

$$z_{12}(t) = \sqrt{R_1^2(A_1^2 + B_1^2) + R_2^2(A_2^2 + B_2^2) - 2R_1 R_2(\cos\Delta\Omega(A_1 A_2 + B_1 B_2) + \sin\Delta\Omega(A_1 B_2 - B_1 A_2)} \Rightarrow$$

$$z_{12}(t) = \sqrt{[R_1 A_1 - R_2\left(A_2\cos\Delta\Omega + B_2\sin\Delta\Omega\right)]^2 + [R_1 B_1 - R_2\left(-A_2\sin\Delta\Omega + B_2\cos\Delta\Omega\right)]^2}$$
$$(3.3)$$

where:

$$\Delta\Omega = \Omega_1 - \Omega_2, \quad R_j = R_j(t) = \frac{a_j(1 - e_j^2)}{1 + e_j\cos f_j(t)}$$

$$A_j = A_j(t) = \cos(f_j(t) + \omega_j), \quad B_j = B_j(t) = \sin(f_j(t) + \omega_j)\cos i_j$$

Given the orbital elements P_j, a_j, e_j, i_j, ω_j, Ω_j and the mid-transit points t_{mtp_j} we can calculate the true anomalies $f_j(t)$ following the same steps that we followed in the previous chapter and finally the projected distances $z_1(t)$, $z_2(t)$ and $z_{12}(t)$ using equations 3.2 and 3.3.

(using equations 2.11, 2.12 and 2.13 to find the time of periastron, t_0, then solving numerically equation 2.14 to find the eccentric anomalies, $E_j(t)$, and then using equation 2.15)
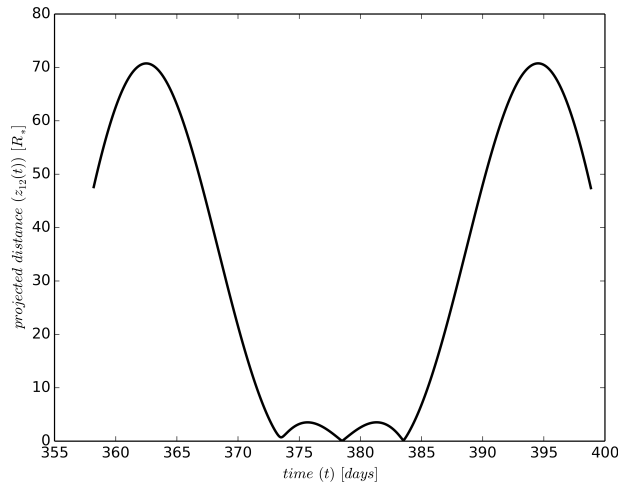
Figure 3.1: *The projected distance of two planets in the same system. Properties of planet 1:* $P_1 = 22.343days$, $a_1 = 26.099R_*$, $e_1 = 0$, $i_1 = 89.383^o$, $\omega_1 = 0^o$, $\Omega_1 = 0^o$, $t_{mtp_1} = 132.74052days$ *and* $p_1 = 0.069R_*$. *Properties of planet 2:* $P_2 = 54.320days$, $a_2 = 47.079R_*$, $e_2 = 0$, $i_2 = 89.560^o$, $\omega_2 = 0^o$, $\Omega_2 = 1.04^o$, $t_{mtp_2} = 161.2379days$ *and* $p_2 = 0.041R_*$.
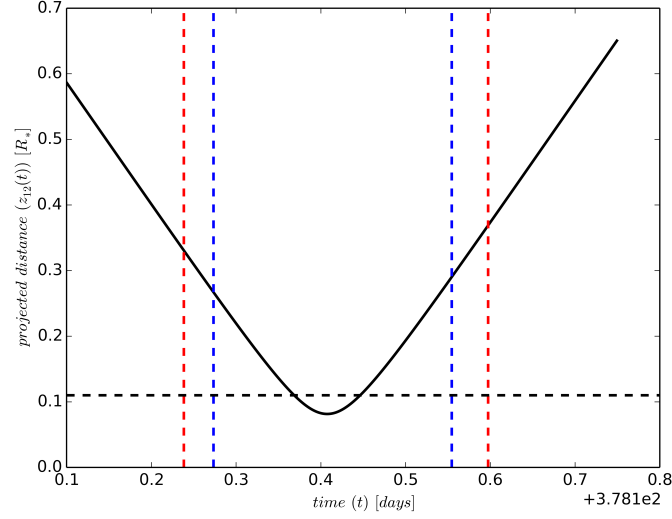
Figure 3.2: Taking a better view at the center of figure 3.1. The vertical blue and red dashed lines are the moments when the transits of the first and the second planet begin and finish. The horizontal black dashed line is the limit $p_1 + p_2$ for the double transit to occur.

3.2 The flux-rise function

After the projected distances we have to calculate the relative flux. During an overlapping double transit the relative flux of the host star will be:

$$F(t) = 1 - \Delta F_1(p_1, z_1(t)) - \Delta F_2(p_2, z_2(t)) + \Delta F_{12}(p_1, z_1(t), p_2, z_2(t), z_{12}(t)) \qquad (3.4)$$

where $\Delta F_1(p_1, z_1(t))$ and $\Delta F_2(p_2, z_2(t))$ are the flux-drops caused by each of the two planets and calculated as described in the previous chapter and $\Delta F_{12}(p_1, z_1(t), p_2, z_2(t), z_{12}(t))$ is the flux-rise caused when the one planet eclipses the other. Actually, the flux-rise is the percentage of the stellar flux that is hidden by both planets. It is included in both flux-drops and as a result it is being subtracted twice. Therefore, we have to add it again if we want our light-curve to be correct.

A flux-rise exists only if:

$$z_1(t) < p_1 + 1 \quad \text{and} \quad z_2(t) < p_2 + 1 \quad \text{and} \quad z_{12}(t) < p_1 + p_2 \qquad (3.5)$$

In the rare case that $z_{12}(t) < max(p_1, p_2) - min(p_1, p_2)$ then the flux-rise equals to the flux-drop of the smaller planet as calculated in chapter 2. In any other case having find the projected distances we can place the three bodies on a polar coordinate system as three circles:

- Star : with $R = 1$ centred at $(0, 0)$;

- Planet with the larger radius : with $R = p_1$ centred at $(z_1(t), 0)$; and

- Planet with the smaller radius : with $R = p_2$ centred at $(z_2(t), cos^{-1}(\frac{z_{12}(t)^2 - z_1(t)^2 - z_2(t)^2}{-2z_1(t)z_2(t)}))$ or at $(z_2(t), 0)$ if $z_1(t) = 0$ or $z_2(t) = 0$;

$\Delta F_{12}(p_1, z_1, p_2, z_2, z_{12})$ will be the integrate of the limb-darkening function inside all the three circles. Each circle is defined by two brunches in polar coordinates if $z_i > p_i$:

- Star : $r = 1$

- Planets: $r_i = p_i$ if $z_i = 0$, $r_i = z_i \cos(u - th_i) + \sqrt{p_i^2 - (z_i \sin(u - th_i))^2}$ if $z_i \le p_i$, $r_i = z_i \cos(u - th_i) \pm \sqrt{p_i^2 - (z_i \sin(u - th_i))^2}$ else

We define as critical points for a circle (u_j) the limits of the two brunches (if they exist) and the its intersections with the other two circles. These points divide each circle into regions . Each region contributes to the final result by:

$$A_j = \pm \frac{1}{F_0} \int_{u_j 1}^{u_j 2} A(r_j) du \qquad (3.6)$$

where $A(r)$ and F_0 are defined in chapter 2 and $\pm$ is decided by where r_j belongs to the positive or the negative brunch (if they exist, if they are not it is positive).

In the case that $z_1 <= p_1$ and $z_2 <= p_2$ only positive brunches exist but in these case the contribution of each region is:

$$A_j = \frac{1}{F_0} \int_{u_j 1}^{u_j 2} A(r_j) du - \frac{1}{F_0} \int_{u_j 1}^{u_j 2} A(0) du \qquad (3.7)$$

Finally, the stars' regions exist only when $z_1 > 1 - p_1$ and $z_2 > 1 - p_2$ and each one contribute to the final result only if it is inside the other two circles with:

$$A_j = \frac{1}{F_0} \int_{u_j 1}^{u_j 2} A(1) du \qquad (3.8)$$

Chapter 4

Applying Models

Each model produces a light-curve based on a set of parameters which we give as input. The number of these parameters has no limit and depends on the complexity of the phenomenon that causes the light-curve and the accuracy of the model, the more accurate that we want our model to be the more the parameters that we have to use. In the previous chapters we explained how the light-curves of some phenomena can be reproduced. More specifically, we worked on the transit light-curve, the double transit light-curve and the light-curve of a system with one transiting and one non-transiting planet. The parameters of each one are many because each planet has 6 orbital parameters plus the mid-transit point, if it is a transiting one, and as a result our models have 7 or 14 parameters.

No matter how accurate our models are, they are useless if we do not have a real light-curve to compare them with. This comparison is called the fitting process and tell us which set of parameters, best reproduces the observed light-curve. The models of the phenomena that we discussed about do not have a continuous analytic expression because of the different cases in the calculation of the integrates. As a result we cannot use some common analytic fitting techniques but we have to produce the model again and again for different sets of parameters and find which one best fits our data. The best fit is the one that has least χ-square:

$$\chi^2 = \sum \frac{(x_j^{obs} - x_j^{mod})^2}{\sigma_j^2} \tag{4.1}$$

This process is called Monte Carlo (MC) fitting and requires a lot of computational power especially if the number of the parameters is so big.

Fortunately, these phenomena are periodical, so, if we observe a system for a long period of time and have a long light-curve we can find the period and reduce the unknown parameters of our model. The period can be found using some well known techniques called periodograms which analyse the light-curve and give us the probability of each period or, as it is known, the frequency spectrum. Fast Fourier Transform (FFT) is a very common periodogram but for us it is not so useful because the light-curves are usually incomplete or unevenly sampled. Determining cycles in such series is not directly possible with methods such as FFT and may require some degree of interpolation to fill in gaps. Instead, we will use the Lomb-Scargle periodogram (or least-squares spectral analysis, LSSA), which estimates a

frequency spectrum based on a least squares fit of sinusoid. An other periodogram which will discuss, but not use, is the Box Least Squares (BLS) periodogram which was developed especially for finding the period of a transit light-curve and, as its name indicates, it estimates a frequency spectrum based on a least squares fit of a rectangular pulse.

4.1 Periodograms

4.1.1 Lomb-Scargle periodogram

Lomb (1976) and Scargle (1982) developed a type of periodogram analysis quite powerful for finding and testing the significance of weak periodic signals in unevenly sampled data.It is equivalent to fitting sine waves of the form $y = a\cos\omega t + b\sin\omega t$. While standard fitting procedures require the solution of a set of linear equations for each sampled frequency, the Lomb-Scargle method provides an analytic solution and is therefore both convenient to use and efficient. The equation for the periodogram was given by Barning (1963), and also Lomb (1976) and Scargle (1982), who furthermore investigated its statistical behaviour, especially the statistical significance of the detection of a signal.

Consider a time series (t_i, y_i), the normalised power of the Lomb-Scargle periodogram will be given by the expression:

$$P(\omega) = \frac{1}{2\sigma^2}\left\{\frac{\left[\sum_i(y_i-\mu)\cos\omega(t_i-\tau)\right]^2}{\sum_i\cos^2\omega(t_i-\tau)} + \frac{\left[\sum_i(y_i-\mu)\sin\omega(t_i-\tau)\right]^2}{\sum_i\sin^2\omega(t_i-\tau)}\right\} \qquad (4.2)$$

where μ and σ are the mean and the standard deviation of the data sample and τ is calculated from the expression:

$$\tan 2\omega\tau = \frac{\sum_i\sin 2\omega t_i}{\sum_i\cos 2\omega t_i}$$

This periodogram is very powerful for unevenly sampled data but also has two problems. First, it does not take into account the error in each measurement and, second, it assumes that the mean of the data and the mean of the fitted sine function are the same. This two problems can be solved by introducing weighted sums (Gilliland & Baliunas 1987), (Irwin et al. 1989) and by fitting the more general function $y = a\cos\omega t + b\sin\omega t + c$ (Zechmeister & Kurster 2009) respectively.

4.1.2 BLS periodogram

The Box Least Squares periodogram (Kovacs et al. 2002) was developed to find periodicity in transit light-curves. Lets say that we have a light-curve containing a periodically repeated transit with period P. From the light-curve we can construct a phase curve which can be represented by a step function:

$$f(t) = \left\{\begin{array}{ll} 1 & \text{if } t < t_0 - \frac{q}{2}P \\ 1-d & \text{if } t > t_0 + \frac{q}{2}P \end{array}\right. \qquad (4.3)$$

where d is the depth of the transit, $t0$ the center of the transit and q the ratio of the transit duration over the period P.

We can simply describe BLS as a procedure which, for every trial period P_0, fits the above step function for different values of d, q and t_0 and returns a value SR, denoting the quality of the fitting. The trial period for which the SR factor becomes maximum is the correct period of the transit. As it can be seen in figure , BLS is a very powerful periodogram for detecting transits, even those with signal compared to the noise level.
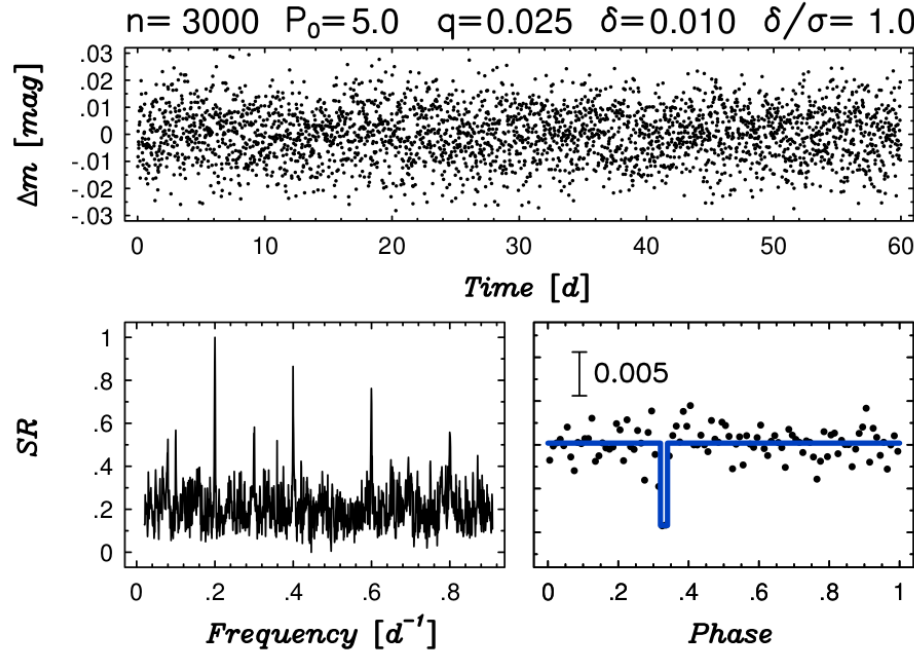

Figure 4.1: BLS test (Kovacs et al. 2002).

4.2   Model fitting

4.2.1   Monte Carlo fitting process

Suppose we have an observed light-curve $(t_j, x_j^{obs} \pm \sigma_j)$ and we want to find the parameters of the system that produces this data. Since a model function is not continuous and analytic, just like the transit model function, we cannot find the set of parameters that reproduces in the best possible way our observational data using analytical methods. The technique that we will use is the Monte Carlo fitting, and the steps that we will follow are:

- Pick some initial sets of parameters (walkers) based on previous research or an educated guess.

- Set the limits and the steps of search for each parameter again based on previous research or an educated guess.

- For each walker, calculate χ-square (equation 4.1).

- For each walker, pick some other sets of parameters (paths) around it, based on the given steps for each parameter, and calculate χ-square.

- Move each walker to the path with the minimum χ-square.

- If a walker cannot find a better path narrow down the steps (for this specific walker).

- If the walker still cannot find a better path widen the steps (for this specific walker) to avoid possible local minima.

- Choose among the walkers the one that has reached the path with the absolute minimum χ-square.

4.2.2 Bootstrap method for error calculation

The bootstrap is a method for calculating the error of the final model parameters exported by the Monte Carlo fitting. Having found the best set of parameters we can reproduce the observed light-curve but, of course, not perfectly because the residuals $x_j^{obs} - x_j^{mod}$ will not be a straight line but a normal distribution with zero mean value and uncertainty:

$$\sigma_{total} = \sqrt{< (x_j^{obs} - x_j^{mod})^2 >} \tag{4.4}$$

We can use σ_{total} to find the errors of the model parameters following the next steps:

- Produce a considerable number of artificial light-curves by adding a normal distribution with zero mean value and uncertainty σ_{total} to the final, best, model.

- Fit again each artificial light-curve and collect a sample for each parameter.

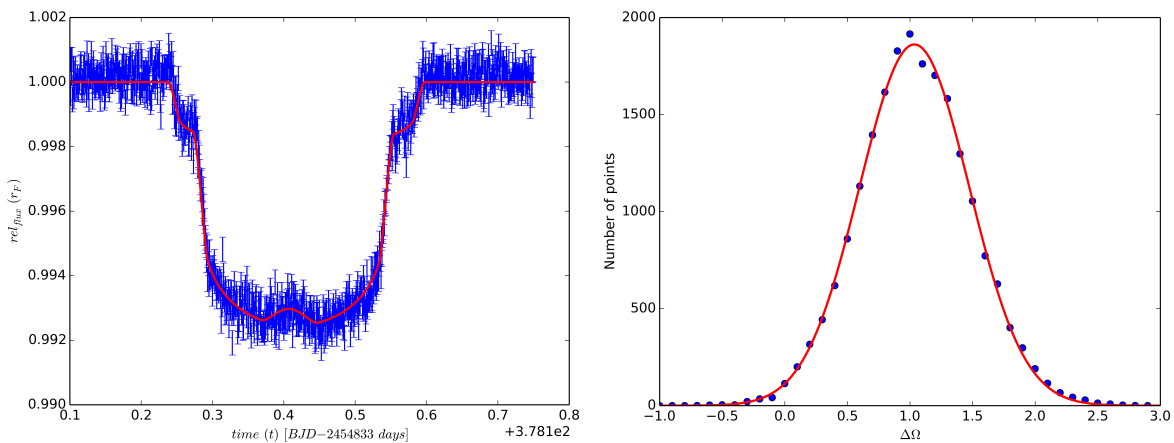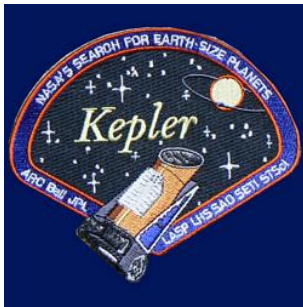- Find the uncertainty for each parameter from each sample.

Figure 4.2: Single parameter fitting and bootstrap distribution.

Chapter 5

Kepler Data

5.1 The Kepler mission

In 1992, NASA proposed a new line of missions to address questions about the Solar System and that would also consider the search for exoplanets. For this opportunity, a team was organized to propose a transit search for terrestrial planets. The proposed concept was called FRESIP (FRequency of Earth-Size Inner Planets) to describe its goal.

After some years of tests and rejected proposals, in 1999, the Kepler test bed was designed, built, and tested (Koch et al. 2000). The results were satisfactory and finally the Kepler mission was selected by NASA as Discovery Mission #10 in December 2001.

Following the discovery of transiting exoplanets, Kepler, was proposed as the tool to find Earth-like exoplanets and give us the opportunity to discover the frequency of such planets in our neighbourhood. This could be achieved by surveying the photometric light-curves of a large sample of stars in order to:

- Determine the abundance of terrestrial and larger planets in or near the habitable zone of a wide variety of stars;

- Determine the distribution of sizes and shapes of the orbits of these planets;

- Estimate how many planets there are in multiple-star systems;

- Determine the variety of orbit sizes and planet reflectivities, sizes, masses and densities of short-period giant planets;

- Identify additional members of each discovered planetary system using other techniques; and

- Determine the properties of those stars that harbour planetary systems.

Although there were ground-based projects surveying for transiting exoplanets, a space-based project would have the photometric precision needed to reliably see

31

an Earth-like transit and to avoid interruptions caused by day-night cycles, seasonal cycles and atmospheric perturbations, such as extinction.

Moreover, this mission should be operated for as long as possible in order to:

- Improve the signal to noise ratio by combining more transits to permit detection of smaller planets;

- Find planets in orbits with larger periods; and

- Find planets around stars that are noisier either due to being fainter or having more variability.

5.1.1   Spacecraft

The spacecraft (figure 5.1) has a mass of $1039kg$ and contains a $1.4m$ primary mirror feeding an aperture of $0.95m$, at the time of its launch this was the largest mirror on any telescope outside Earth orbit. The photometer has a soft focus to provide excellent photometry, rather than sharp images. The mission goal is a combined differential photometric precision (CDPP) of $20ppm$ for a $m_V = 12$ solar-like star. Given for comparison, an Earth-like transit produces a brightness change of $84ppm$ and lasts for thirteen hours when it crosses the center of the star.

The focal plane of the spacecraft's camera is made up of 42 CCDs at 2200×1024 pixels, which made it at the time the largest camera yet launched into space, possessing a total resolution of 95 mega-pixels. The bandpass of the camera is $430 - 890nm$.

5.1.2   Launch and orbit

The Kepler observatory was launched on March 7, 2009 at 03:49:57 UTC aboard a Delta II rocket from Cape Canaveral Air Force Station, Florida. The launch was a complete success and all three stages were completed by 04:55 UTC. The cover of the telescope was jettisoned on April 7, 2009, and the first light images were taken on the next day.

Kepler orbits the sun a little bit further than Earth and looks always vertically to its orbit in order to avoid the sunlight. It also rolls 90 degrees about the line-of-sight every 3 months for the same reason.

Figure 5.1: The Kepler spacecraft.

5.1.3   Field of view

The photometer of Kepler points to a field in the northern constellations of Cygnus, Lyra and Draco, which is well out of the ecliptic plane, so that sunlight never enters the photometer as the spacecraft orbits the Sun. This is also the direction of the
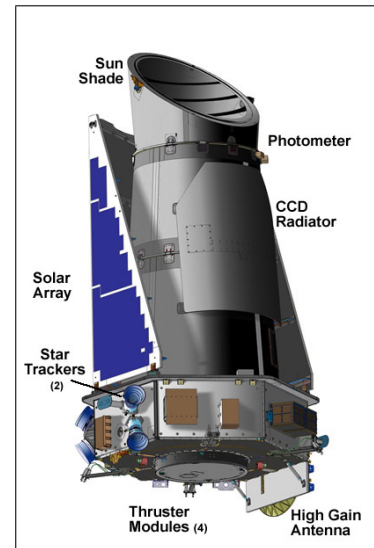
Solar System's motion around the center of the galaxy. Thus, the stars which Kepler observes are roughly the same distance from the galactic center as the Solar System, and also close to the galactic plane. Kepler's field of view covers 100 square degrees, around 0.25 percent of the sky.

Figure 5.2: Kepler's field of view.

5.1.4 Discoveries

Until today Kepler has published light-curves of almost 200000 stars in 17 packages one for each 3-months period (quarter). In side these data almost 1000 new confirmed planets have been found and there are an other 3000 waiting to be confirmed. On April 17, 2014, the Kepler team announced the discovery of Kepler-186f, the first nearly Earth-sized planet located in the habitable zone orbiting around a red dwarf star.
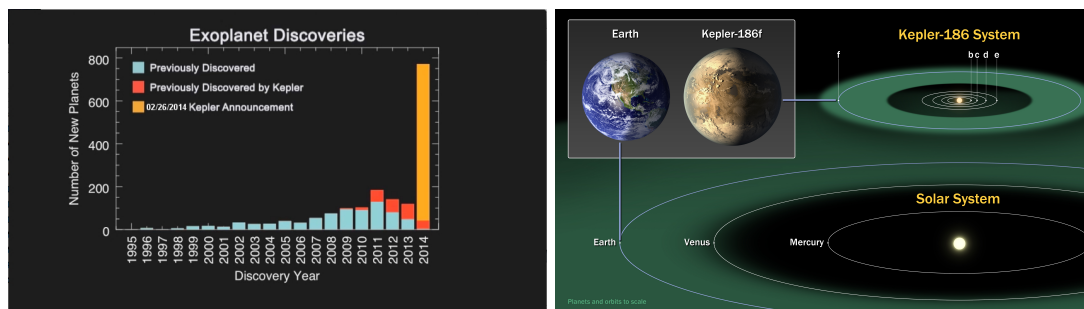

Figure 5.3: Kepler's discoveries.

5.2 Data retrieval and de-trending

Each star in the Kepler field has a KID number (Kepler ID) and those that may have in their light-curves transit events have KOI number (Kepler Object of Interest). There are two kinds of light-curves for each target one llc (long cadence light-curve) with data points separated by thirty minutes and one slc (sort cadence light-curve) with data points separated by one minute. These data are in fits format and contain two kinds of data, the SAP and the PDC data. The PDC light-curves are corrected

in order to remove systematic errors. Kepler data can be downloaded via MAST archives website.

We downloaded all KOI light-curves in order to study some of them but there was one more step that we had to take. Kepler photometry is very precise and as a result light-curves from Kepler contain stellar activity variations (trends) which have to be removed in order to study only the transits.

For these purpose we developed a simple software for de-trending the llc PDC light-curves without using the periods of each planet. The steps that our code follows are:

- Its goal is to fit a polynomial (of 5th power) excluding the transit points from the fitting process.

- Constructs the distribution of the differences between subsequent points.

- Checks all the points that differ from their previous more than two time the sigma of the distribution.

- If such a point is isolated it is characterised as a jump point and it is excluded from the fitting.

- If this difference is due to time gap or a jump with different continuous light-curves before and after its is characterised as a split point and at this point the fitting process stops and starts again.

- If none of the above is true then it is characterised as a transit point and all the following points are excluded from the fitting until the light-curve becomes continuous again.

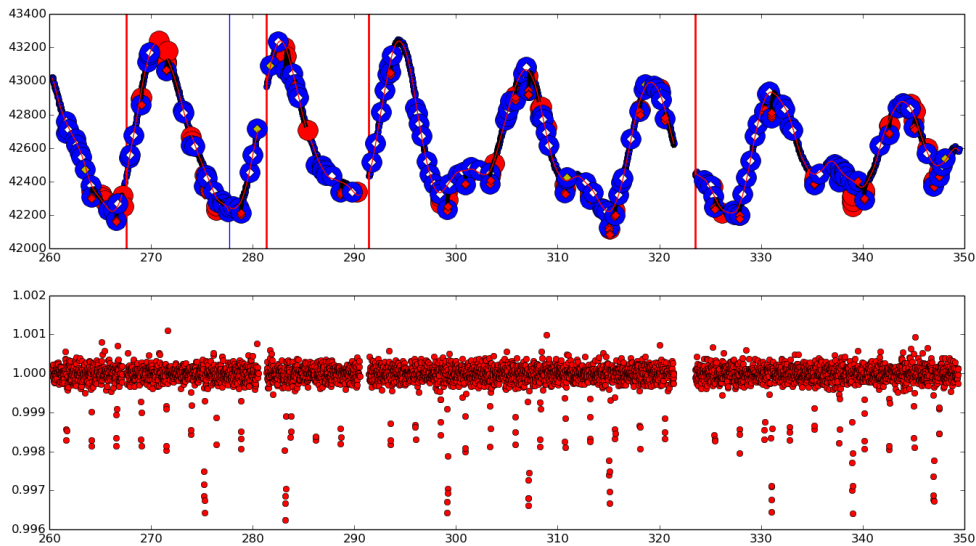An example can be seen in the next figure (5.4).

Figure 5.4: LLc de-trending.

5.3 Overlapping double transits in Kepler data

We tried to find cases inside the Kepler data when an overlapping double transit took place in order to calculate the mutual inclination between the orbits of the planetary companions. In this section we will discuss the way we found the candidates from the KOIs and the results of fitting our model on their light-curves.

5.3.1 The survey

At first we had to find all the possible systems that may appear to have an overlapping double transit with magnitude that could be separated from the noise of the light-curve. Based on that, we chose all light-curves (table 5.1) with two or more planetary candidates (or confirmed planets) which had a model signal-to-noise ratio (SNR) higher than 150 (as provided by the Kepler team).

Table 5.1: Light-curves with two or more planetary candidates with $SNR > 150$.

KID	KOI_1	KOI_2	SNR_1	SNR_2
4349452	244.01	244.02	293.1	387.4
6462863	94.01	94.03	225.8	562.4
7447200	676.01	676.02	326.4	352.2
8644288	137.01	137.02	233.6	448.0
9471974	119.01	119.02	159.2	314.2
9946525	398.01	398.02	156.4	313.0
10723750	209.01	209.02	324.6	409.5
10937029	433.01	433.02	160.4	319.0
11253827	2672.01	2672.02	170.4	286.3
11442793	351.01	351.02	212.8	217.4
11773022	620.01	620.02	181.8	412.4
11904151	72.01	72.02	162.1	193.4

For each of the these light-curves we used the transit period P_j and the first mid-transit point t_{j0}^m provided by the Kepler team for each KOI to find all the mid-transit points t_j^m until the end of the light-curve:

$$t_1^m = t_{10}^m + N_1 P_1 \quad t_2^m = t_{20}^m + N_2 P_2 \quad \text{for} \quad N_1, N_2 = 0, 1, 2, \ldots \tag{5.1}$$

From the two lists we kept only those couples when the two planets were simultaneously transiting the host star (overlaps) depended on the duration D_j of each transit provided by the Kepler team:

$$\mid t_{1k}^m - t_{2l}^m \mid < \frac{D_1 + D_2}{2} \tag{5.2}$$

To choose which of these overlaps should be investigated further we used the factor:

$$O_f = \frac{\left[\min(t_1^f, t_2^f) - \max(t_1^i, t_2^i) \right]^2}{D_1 D_2} \tag{5.3}$$

where $\min(t_1^f, t_2^f) - \max(t_1^i, t_2^i)$ indicates the duration of the overlap, so O_f gives the duration of the overlap in relation with each transit duration. In the ideal case of two transits with identical t_j^m and D_j, O_f would be equal to 1 . We decided to investigate all those overlaps with $O_f > 0.5$.

The final step was to find the actual parts of the light-curves because they are not continuous and some of the prospective overlaps may were missing. As mentioned above there are two sets of data for each KOI object, the long and the short cadence, in which data points are separated by thirty and one minute respectively. For an overlapping double transit to be seen we needed the short cadence light-curve. In table 5.2 all the overlaps with good probability for a double transit are listed.

One problem with the method just described is that it dose not take into account possible time variations assuming that the time intervals between transits are fixed and equal to the transit period. Unfortunately there is no way to perform a quick survey for overlapping double transits and solve this problems. For KOIs with large TTVs a different procedure should be followed.

Table 5.2: Overlaps with good probability for a double transit.

KID	KOI_1	KOI_2	t_{1k}^m	t_{2l}^m	O_f
4349452	K00244.02	K00244.01	801.7990793	801.825295	0.65232207952
6462863	K00094.03	K00094.01	378.5197	378.513481	0.788599413724
7447200	K00676.01	K00676.02	1566.77847	1566.7815291	0.590938423397
7447200	K00676.01	K00676.02	992.7553308	992.7247965	0.505539568705
7447200	K00676.01	K00676.02	1279.7669004	1279.7531628	0.590938423397
7447200	K00676.01	K00676.02	1343.5472492	1343.5372442	0.590938423397
7447200	K00676.01	K00676.02	1247.876726	1247.8611221	0.590938423397
7447200	K00676.01	K00676.02	1375.4374236	1375.4292849	0.590938423397
7447200	K00676.01	K00676.02	1407.327598	1407.3213256	0.590938423397
7447200	K00676.01	K00676.02	1311.6570748	1311.6452035	0.590938423397
7447200	K00676.01	K00676.02	1120.3160284	1120.2929593	0.590938423397
7447200	K00676.01	K00676.02	1439.2177724	1439.2133663	0.590938423397
7447200	K00676.01	K00676.02	1152.2062028	1152.185	0.590938423397
7447200	K00676.01	K00676.02	1534.8882956	1534.8894884	0.590938423397
7447200	K00676.01	K00676.02	1502.9981212	1502.9974477	0.590938423397
7447200	K00676.01	K00676.02	1215.9865516	1215.9690814	0.590938423397
7447200	K00676.01	K00676.02	1088.425854	1088.4009186	0.590938423397
7447200	K00676.01	K00676.02	1056.5356796	1056.5088779	0.563389080969
7447200	K00676.01	K00676.02	1024.6455052	1024.6168372	0.534072692051
8644288	K00137.01	K00137.02	1212.8689146	1212.85534	0.824975220199
8644288	K00137.01	K00137.02	677.9589726	677.9335	0.684955942331
8644288	K00137.01	K00137.02	945.4139436	945.39442	0.753339039524
8644288	K00137.01	K00137.02	410.5040016	410.47258	0.619825928597
9946525	K00398.02	K00398.01	1310.6953248	1310.712816	0.512664746812
11773022	K00620.01	K00620.02	1513.76944	1513.85445	0.526006887282

From these prospective overlaps, finally, two KOIs were found to have distortions similar to a double transit, KOI-94, KOI-620, in the next paragraphs we will discuss the results for each one of them.

5.3.2 Results for KOI-94

The first step was to find the orbital properties of each overlapping planet by fitting our transit model on the phase folded light-curves, assuming that the epoch and period of them are known, as provided by the Kepler team, (limb-darkening coefficients also provided by the Kepler team).

$$KOI - 94.01 \quad 132.74052 + N \times 22.343001[BJD - 2454833]$$

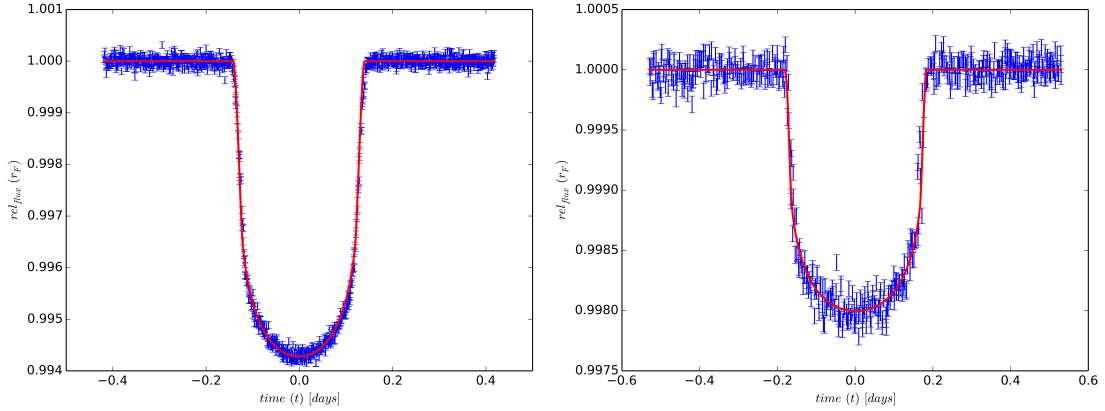$$KOI - 94.03 \quad 161.23790 + N \times 54.319930[BJD - 2454833]$$

Figure 5.5: Phase folded light-curves and fitting for the two overlapping planets in the KOI-94 system.

Table 5.3: Fitted orbital properties of each overlapping planet .

	Hirano et al. (2012)	Masuda (2013)	This work
KOI-94.01			
R_p/R_*	-	0.06954 ± 0.00043	0.069
a/R_*	-	26.21 ± 0.082	26.10
b	-	0.2951 ± 0.0092	-
$i[deg]$	-	-	89.38
$T_0[BJD - 2454833]$	378.51363 ± 0.00024	378.51372 ± 0.00023	-
KOI-94.03			
R_p/R_*	-	0.04123 ± 0.00070	0.041
a/R_*	-	47.44 ± 0.027	47.08
b	-	0.3693 ± 0.0095	-
$i[deg]$	-	-	89.56
$T_0[BJD - 2454833]$	378.51790 ± 0.00062	378.51785 ± 0.00060	-
$\Delta\Omega[deg]$	1.15 ± 0.55	1.13 ± 0.52	1.10 ± 0.39

As we see the results for $\Delta\Omega$ from the three different models are consistent with each other, and so the different orientation of the two orbits is a strong possibility for KOI-94. We have to admit that our smaller error is a result of not including the errors in the orbital parameters.
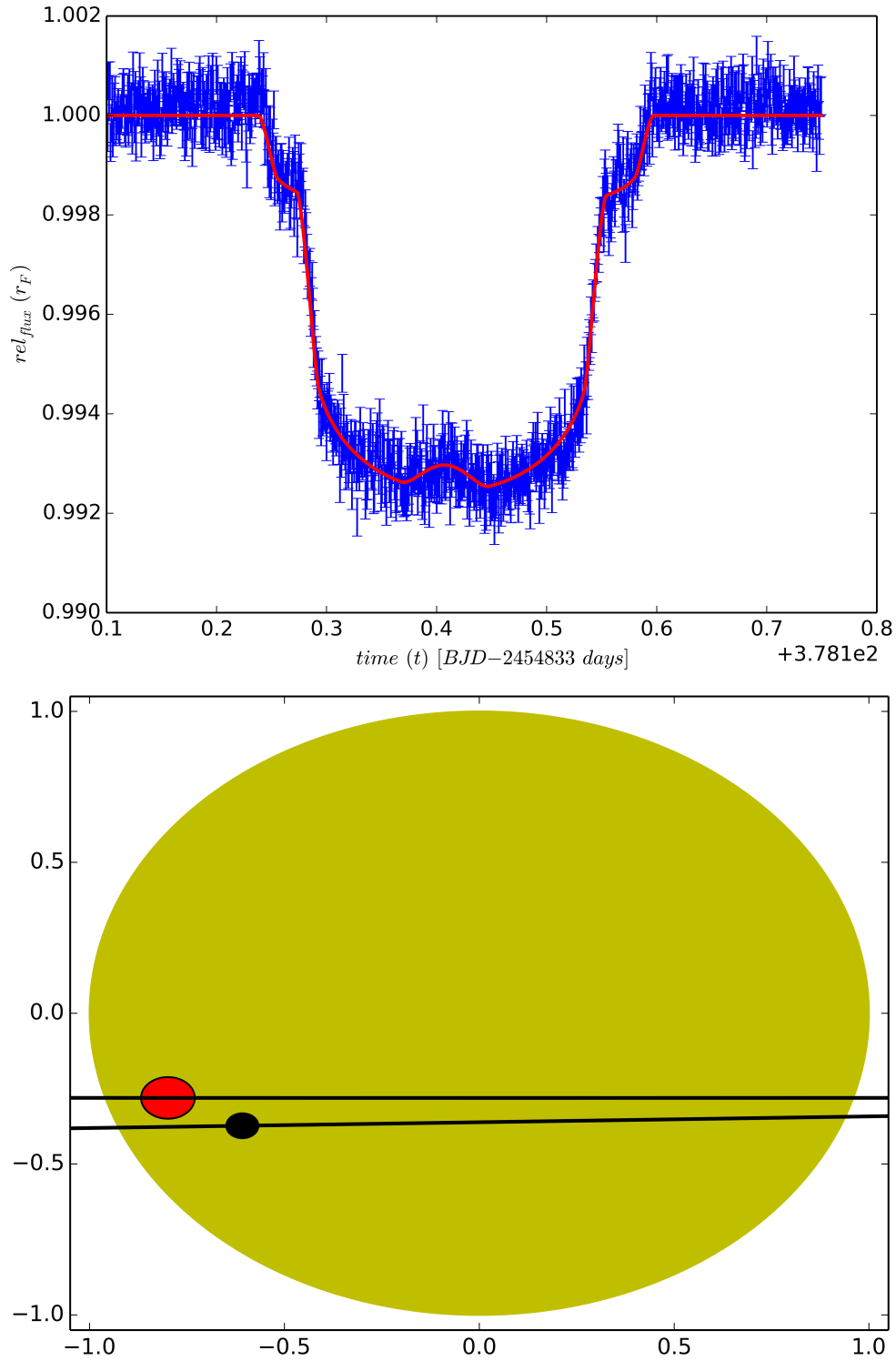
Figure 5.6: Light-curve and geometry of the overlapping transit in KOI-94 system.

5.3.3 Results for KOI-620

The same procedure was follows for KOI-620 too, assuming that the epoch and period of them are known, as provided by the Kepler team, (limb-darkening coefficients also provided by the Kepler team).

$$KOI - 620.01 \quad 159.10435 + N \times 45.155503 [BJD - 2454833]$$

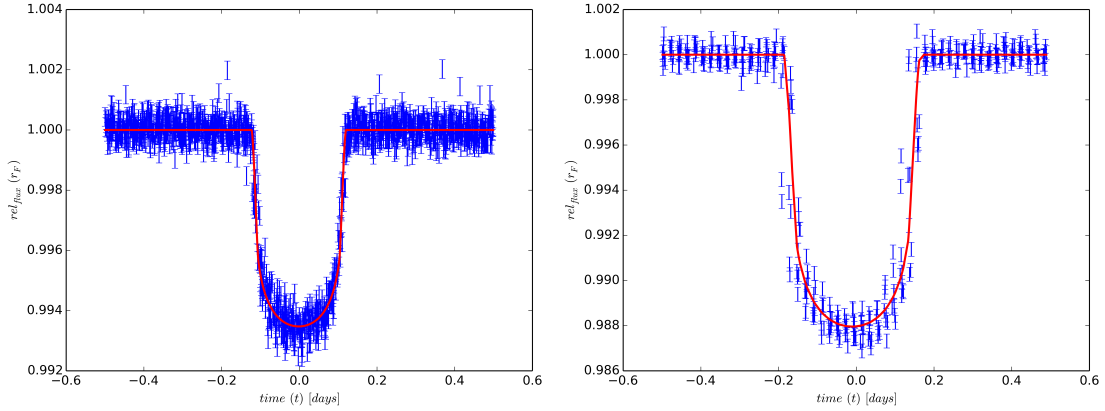$$KOI - 620.02 \quad 212.02345 + N \times 130.1831 [BJD - 2454833]$$

Figure 5.7: Phase folded light-curves and fitting for the two overlapping planets in the KOI-620 system.

Table 5.4: Fitted orbital properties of each overlapping planet .

	Masuda (2013)	This work
KOI-620.01		
R_p/R_*	0.0741 ± 0.00017	0.0738
a/R_*	63.65 ± 0.33	63.49
b	0.016 ± 0.0012	-
$i[deg]$	-	89.97
$T_0[BJD - 2454833]$	1513.76694 ± 0.00083	-
KOI-620.02		
R_p/R_*	0.1019 ± 0.0011	0.1002
a/R_*	128.93 ± 0.66	129.56
b	0.039 ± 0.04	-
$i[deg]$	-	89.97
$T_0[BJD - 2454833]$	1513.78988 ± 0.00070	-
$\Delta\Omega[deg]$	-25.3 ± 6.5	-31.5 ± 2.6

As we see the results for $\Delta\Omega$ from the two different models are not consistent with each other, and so the different orientation of the two orbits is not a strong possibility for KOI-620. The probability of the planets orbiting in such different orbits to be seen as transiting planets is too small. Additionally the existence of the overlapping double transit is tightly connected with the other orbital properties. Masuda (2014) proposed that this light-curve is the effect of a spot but we

still believe that there is a small possibility for overlapping double transit and a spectroscopic observation will answer the question. We, again, have to admit that our smaller error is a result of not including the errors in the orbital parameters.
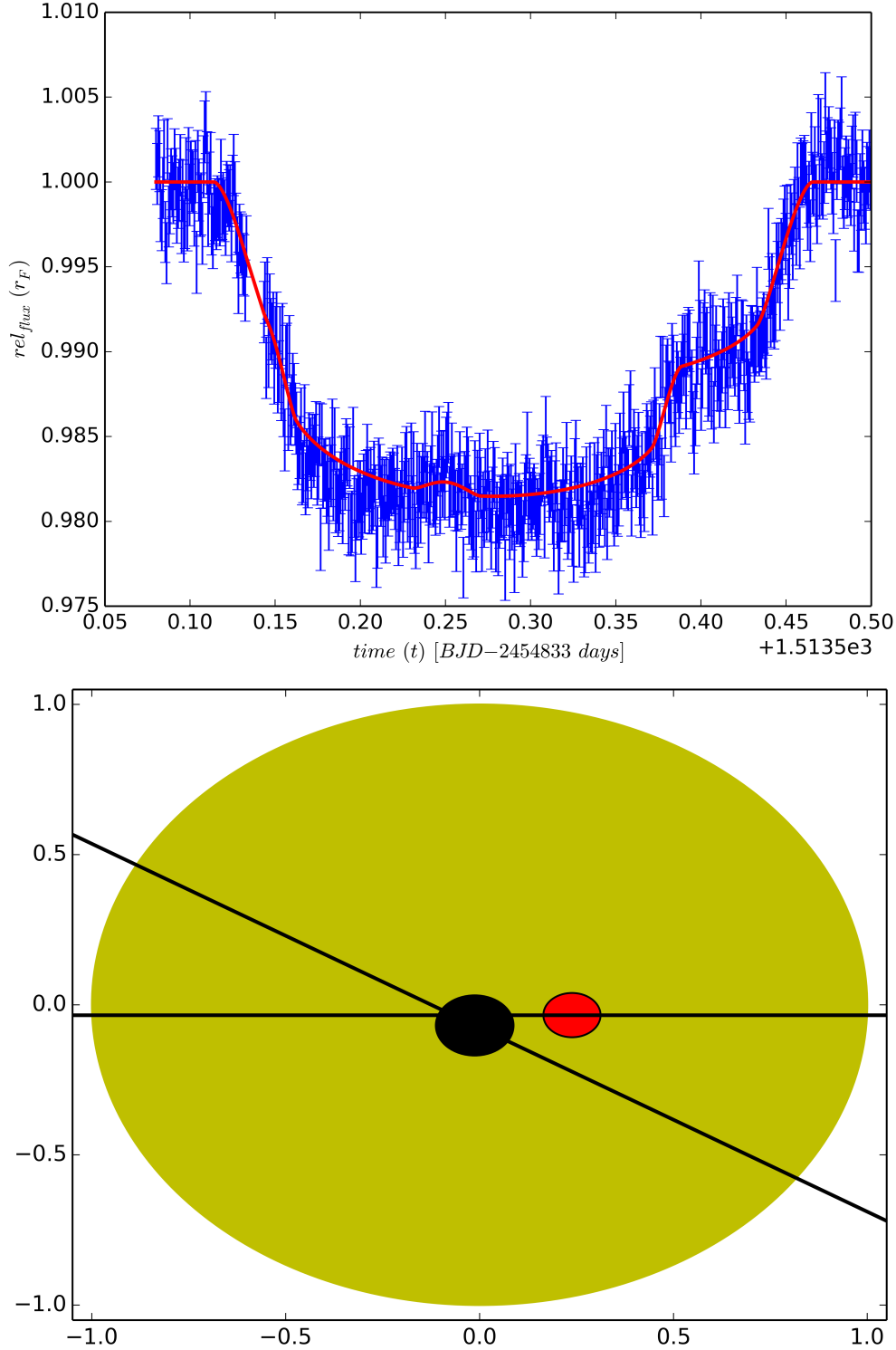

Figure 5.8: Light-curve and geometry of the overlapping transit in KOI-620 system.

5.4 TTVs in Kepler data

We also tried to find cases inside the Kepler data when the times of a transit vary in relation with the expected time of minima. In this section we will discuss the way we found the candidates from the KOIs.

Our goal was to find significant TTVs in transit light-curves of single-planets KOIs (from all the quarters of Kepler data) in order to detect possible non-transiting companions. At first we had to find all the possible light-curves in which TTVs could be detectable. Based on that, we chose all light-curves with transits with depth larger that five time the rms of the light-curve (without the transit points). Then, in order to be quick our survey, tried to fit a parabola and find the observed times of minima. Having all the candidates we then fitted our transit model and used it to point out more accurately the times of minima. Of course most of our candidates were included in the catalogue of Mazeh et al. (2013) but we also found some that were not included and present them together with their periodograms (selectively) in the next figures.
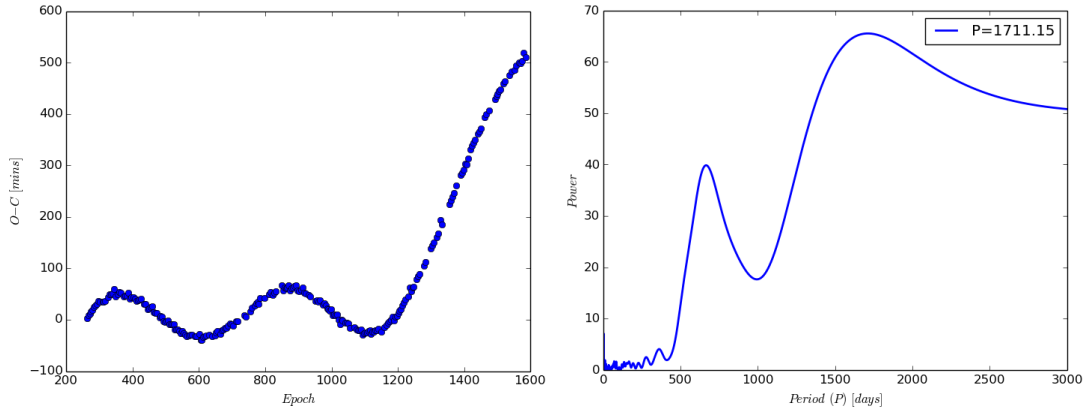

Figure 5.9: O-C and periodogram for KOI-984 (included).
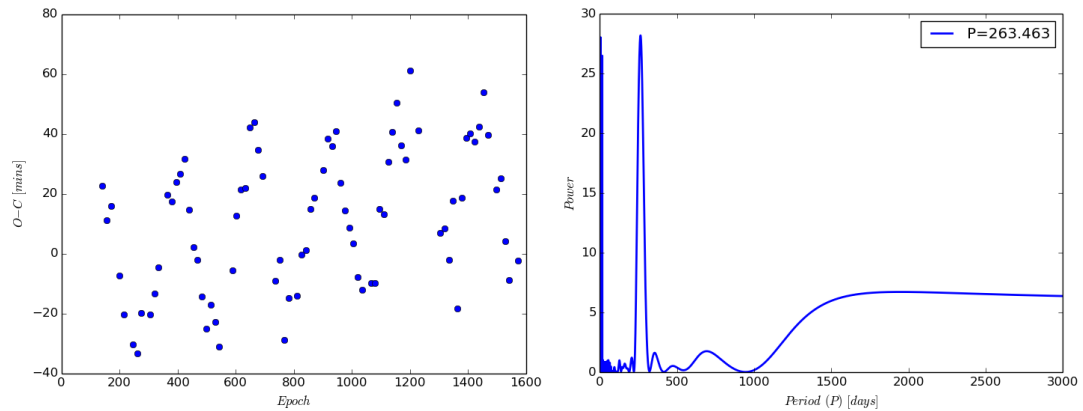

Figure 5.10: O-C and periodogram for KOI-103 (included).
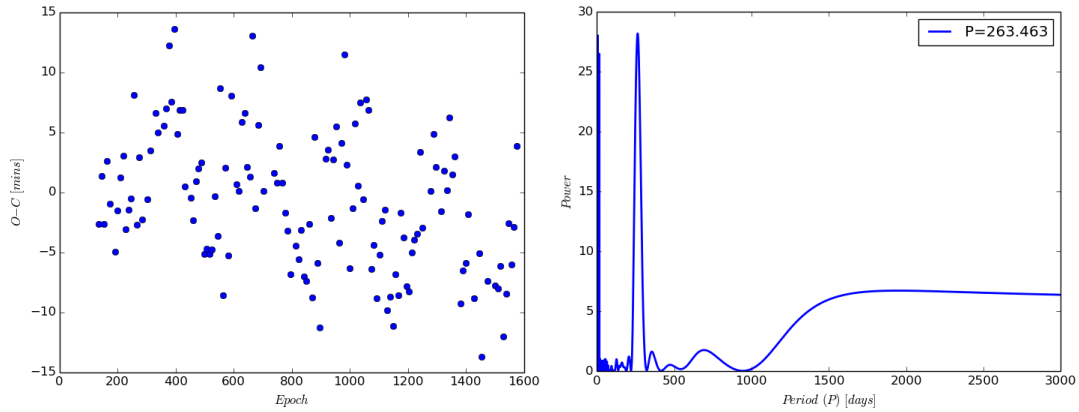
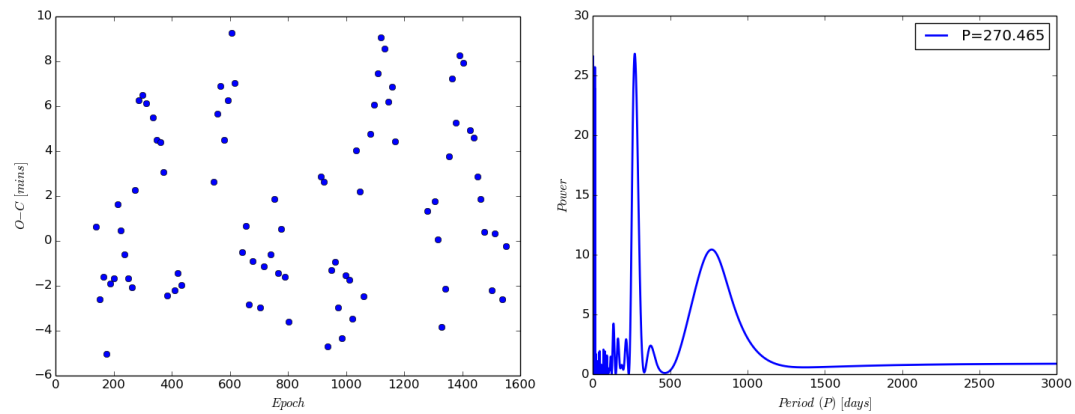Figure 5.11: O-C and periodogram for KOI-84 (included).

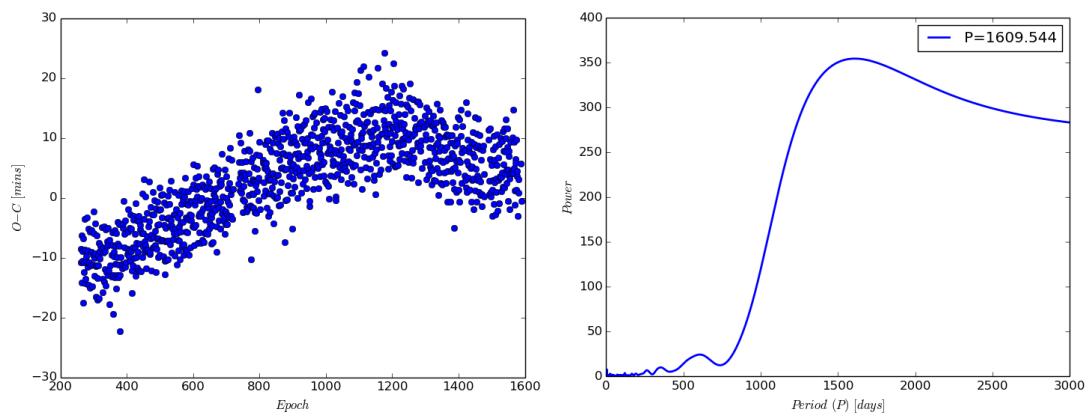Figure 5.12: O-C and periodogram for KOI-190 (included).

Figure 5.13: O-C and periodogram for KOI-3692 (not included).
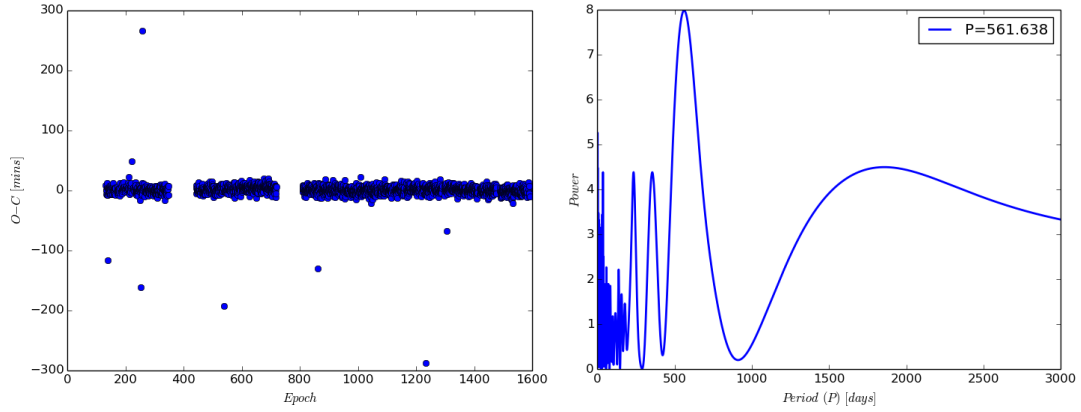
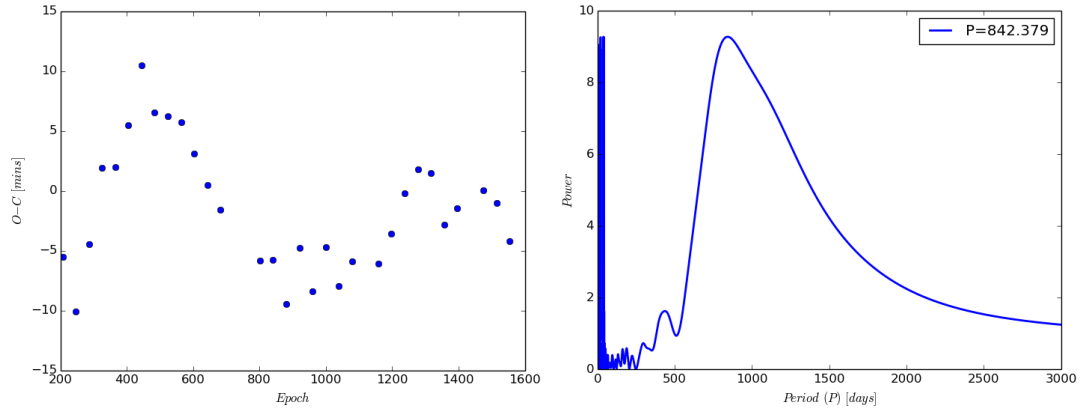Figure 5.14: O-C and periodogram for KOI-2950 (not included).

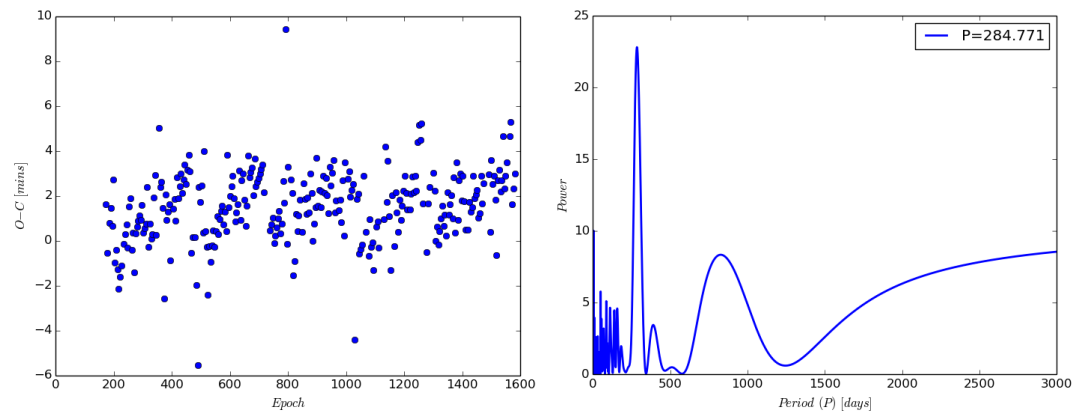Figure 5.15: O-C and periodogram for KOI-918 (included).

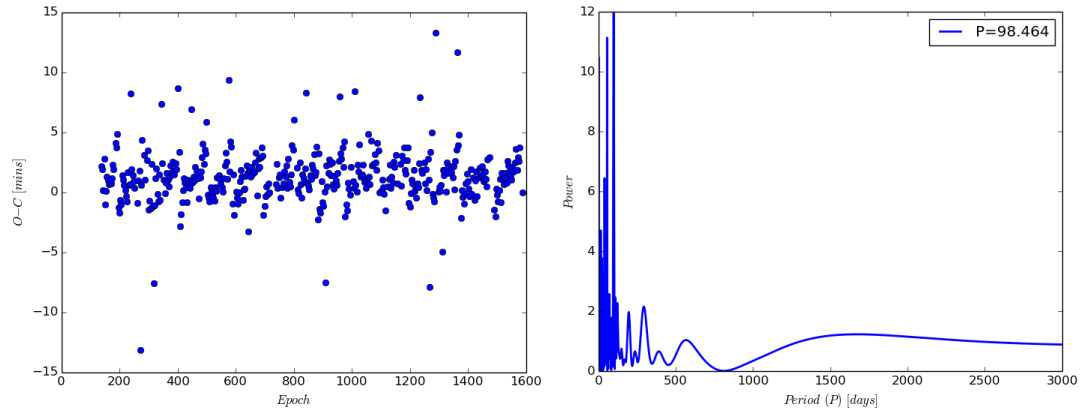Figure 5.16: O-C and periodogram for KOI-421 (not included).

Figure 5.17: O-C and periodogram for KOI-199 (not included).

Chapter 6

Holomon Follow-up Program

6.1 Holomon Observatory

6.1.1 Location

Holomon observatory is operated under the supervision of the Laboratory of Observational Astronomy of the Physics Department of AUTh (Aristotle University of Thessaloniki). Located on Mount Holomon at Chalkidiki, Greece, provides very good seeing conditions for observations to be carried out.
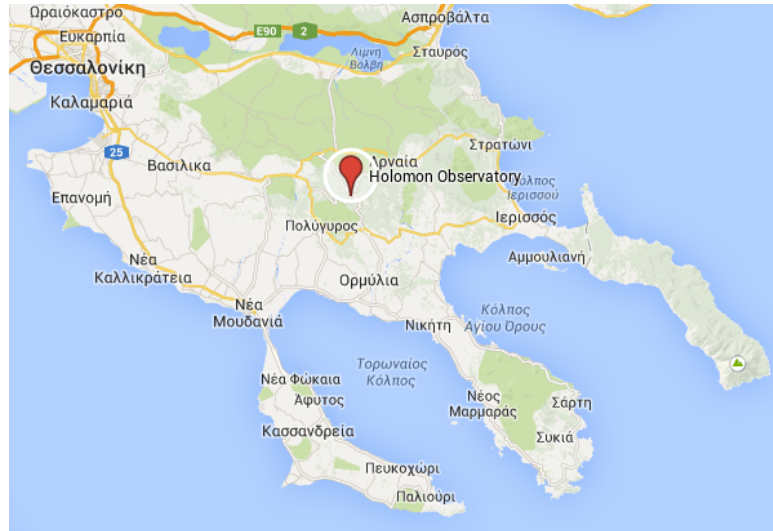

Figure 6.1: Location of Holomon observatory.

6.1.2 Equipment

Holomon observatory is equipped with 3 mounts, 3 telescopes and 3 CCD cameras as described in table 6.1. For our observations we used a Celestron CGE Pro or an Orion Atlas EQ-G mount with a Celestron 11 inch XLT-StarBright telescope and an Atik 11000 CCD camera with binning 2×2 and exposure times of 60 or 90 seconds depending on the conditions.

Table 6.1: Holomon observatory equipment.

type	manufacturer	model
mount	Celestron	CGE Pro
mount	Orion	Altas EQ-G
mount	Sky Watcher	EQ 6 Pro
telescope	Celestron	11 inches XLT-StarBright
telescope	Meade	10 inches LX200
telescope	Takahashi	8 inches E-180 ED
CCD camera	Finger Lakes	FLI 2376 04
CCD camera	Atik	4000
CCD camera	Atik	11000

Figure 6.2: Equipment used for our observations.

6.1.3 Observations overview

The capabilities of the equipment of our observatory and the fact that it is available at any time were the motivations of this project. The idea was that as long as we were able to obtain scientific data any season of the year we could have a considerable number of follow up observations on some already discovered exo-planets in order to study possible perturbations due to an additional, non-transiting exo-planet in the same system. Unfortunately, technical problems, occurred at the beginning of this academic year, did not let us start the observations immediately but only in February 2014. From that period until now (July 2014) the weather in mount Holomon was unstable and as a result we do not have the expected number of observations. Nonetheless, we managed to solve many of these technical issues

and also develop our own software for observations organising and data analysis, and more specifically, photometry.

6.2 Target selection and observations schedule

6.2.1 Target selection

The available equipment and the goal of our observations imposed specific limitations in the selection of possible targets for follow up observations.

- Based on previous experience and tests on the available equipment capabilities and considering the fact that we wanted to have a valid model fitting on each transit light-curve we had to choose a star with $m_V < 14$ and a planet with $transit_{depth} > 10 mmag$.

- In order to have satisfying number of possibly observable transit events our target should have a declination higher than 0° and $transit_{period} < 5 days$.

- Finally, for a whole transit event to be observable during a night plus a considerable fraction of it before and after we chose among those targets with $transit_{duration} < 180 min \quad (3 hours)$.

Based on the above criteria we decided to perform follow up observations on the known hot-Jupiter Qatar-1b (K. A. Alsubai et al. 2010). The field of view can be seen in figure 6.3 and the properties in table 6.2.

Figure 6.3: Field of view of the transiting exo-planet Qatar-1b.

Table 6.2: Qatar-1b system properties.

| Stellar Properties (exoplanets.eu)	
RA	$20^h13^m32^s$
DEC	$+65^o09'43''$
Apparent magnitude	12.86
Spectral type	K
Effective temperature	$4861.0 \pm 125.0K$
Mass	$0.85 \pm 0.03M_\odot$
Radius	$0.823 \pm 0.025R_\odot$
Metallicity [Fe/H]	0.2 ± 0.1
Planet Properties (exoplanets.eu)	
Minimum Mass	$1.09 \pm 0.084M_J$
Radius	$1.164 \pm 0.045R_J$
Transit Properties (exoplanets.eu)	
Primary transit	$2455518.4102HJD$
Period	$1.4200246days$
Depth	$20.4mmag$
Duration	$96.7min$
Model Properties (von Essen et al. 2013)	
Primary transit	$2456157.42204 \pm 0.0001BJD_{TDB}$
Period	$1.4200246 \pm 0.0000004days$
Inclination	$84.52 \pm 0.24deg$
Semi-major axis	$6.42 \pm 0.1R_*$
Planet radius	$0.1435 \pm 0.0008R_*$
Quadratic limb-darkening coefficients	$0.5860 / 0.6025$

6.2.2 Observations schedule
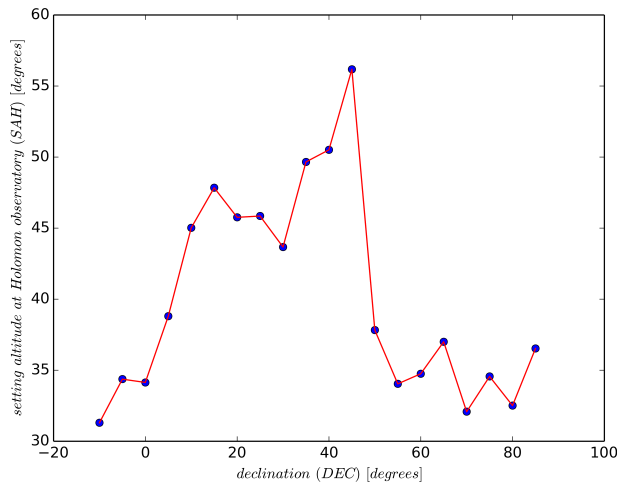
Figure 6.4: Setting horizon for different declinations at Holomon observatory.

Holomon observatory has a disadvantage as far as the location is concerned. Near to the telescopes there are trees blocking the star light come from the west and changing the horizon level (figure 6.4). In order to successfully organise our observations we build a simple program (Holomon Observations Organiser, HObOr) to calculate the time of rise and set for a star at the Holomon observatory, given its coordinates, with respect to the sun-rise, sunset, moon-rise and moon-set. To achieve that we used the python library Py-Ephem. An example of the HObOr output for Qatar-1b can be seen and explained in figure 6.5. Finally in table 6.3 possibly observable transit events of Qatar-1b for 2014 are listed.
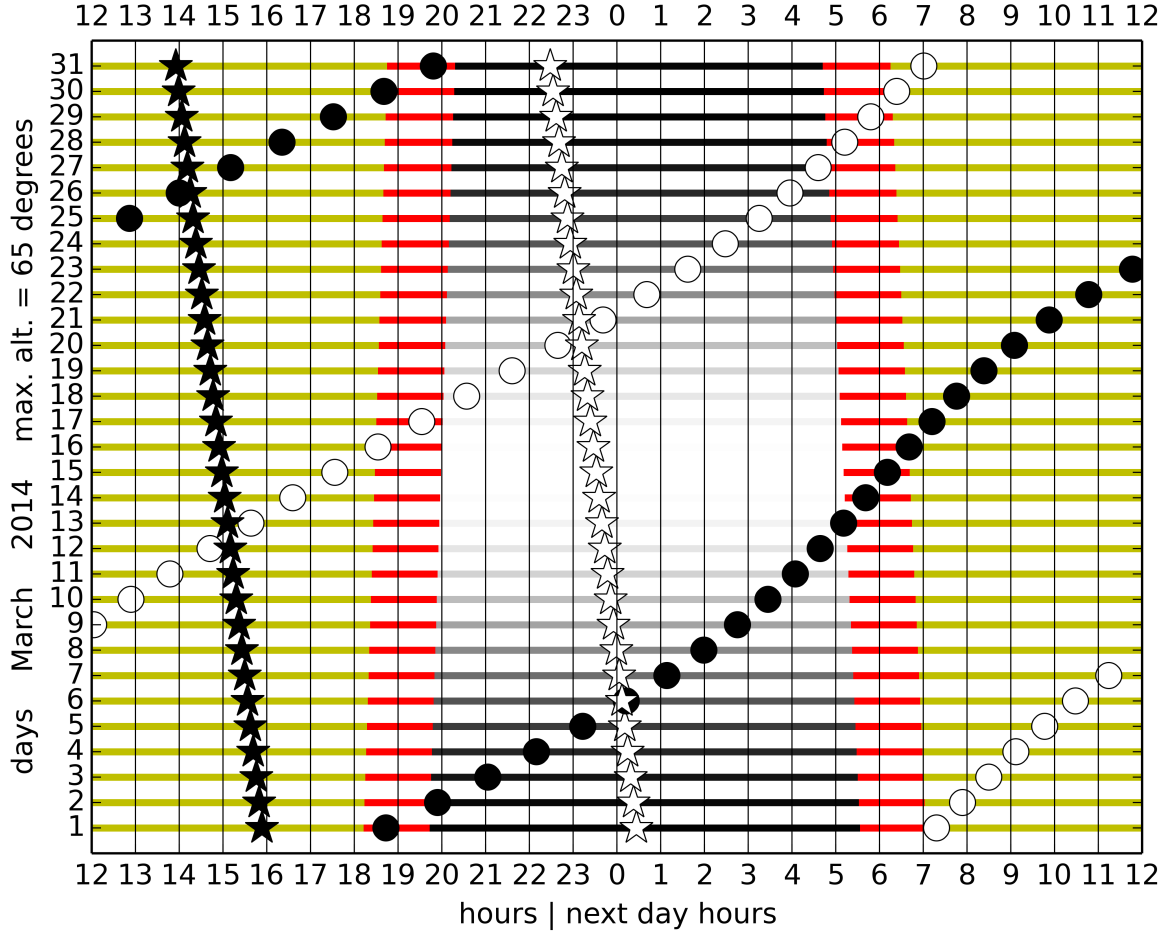
Figure 6.5: Rising and setting of Qatar-1b field of view at Holomon observatory for March 2014. Yellow lines are used for day time,red for twilight and black-scaled for night. "White" are those noghts with full moon and "black" nights those with new moon. White and black circles represent the time of moon-rise and moon-set respectively and white and black stars represent the time of target-rise and target-set respectively.

Table 6.3: Qatar-1b possibly observable transit events for 2014 from Holomon astronomical station by ETD and HObOr.

Mid point HJD	Beginning UT (alt)	Mid point UT (alt)	Ending UT (alt)
2456705.551	17.02 0:24 (24,N)	17.02 1:13 (28,NE)	17.02 2:01 (32,NE)
2456712.651	24.02 2:48 (39,NE)	24.02 3:37 (44,NE)	24.02 4:25 (49,NE)
2456715.491	26.02 22:58 (21,N)	26.02 23:46 (24,N)	27.02 0:35 (28,NE)
2456722.591	06.03 1:22 (34,NE)	06.03 2:11 (39,NE)	06.03 2:59 (44,NE)
2456725.431	08.03 21:32 (19,N)	08.03 22:20 (21,N)	08.03 23:09 (24,N)
2456732.531	15.03 23:56 (30,NE)	16.03 0:44 (34,NE)	16.03 1:33 (39,NE)
2456739.631	23.03 2:20 (47,NE)	23.03 3:09 (52,NE)	23.03 3:57 (57,NE)
2456742.471	25.03 22:30 (26,NE)	25.03 23:18 (30,NE)	26.03 0:07 (35,NE)
2456749.572	02.04 0:54 (42,NE)	02.04 1:43 (47,NE)	02.04 2:31 (52,NE)
2456752.412	04.04 21:04 (23,N)	04.04 21:52 (27,NE)	04.04 22:41 (31,NE)
2456759.512	11.04 23:28 (38,NE)	12.04 0:16 (42,NE)	12.04 1:05 (47,NE)

continue... table 6.3

Mid point HJD	Beginning UT (alt)	Mid point UT (alt)	Ending UT (alt)
2456762.352	14.04 19:38 (20,N)	14.04 20:26 (23,N)	14.04 21:14 (27,NE)
2456766.612	19.04 1:52 (55,NE)	19.04 2:41 (60,NE)	19.04 3:29 (63,N)
2456769.452	21.04 22:02 (33,NE)	21.04 22:50 (38,NE)	21.04 23:39 (43,NE)
2456776.552	29.04 0:26 (50,NE)	29.04 1:14 (55,NE)	29.04 2:03 (60,NE)
2456779.392	01.05 20:36 (29,NE)	01.05 21:24 (33,NE)	01.05 22:12 (38,NE)
2456786.492	08.05 23:00 (46,NE)	08.05 23:48 (51,NE)	09.05 0:37 (55,NE)
2456789.332	11.05 19:10 (25,NE)	11.05 19:58 (29,NE)	11.05 20:46 (33,NE)
2456793.592	16.05 1:24 (62,N)	16.05 2:12 (65,N)	16.05 3:01 (66,N)
2456796.432	18.05 21:34 (41,NE)	18.05 22:22 (46,NE)	18.05 23:10 (51,NE)
2456803.532	25.05 23:58 (58,NE)	26.05 0:46 (62,N)	26.05 1:35 (65,N)
2456806.373	28.05 20:08 (36,NE)	28.05 20:56 (41,NE)	28.05 21:44 (46,NE)
2456813.473	04.06 22:32 (54,NE)	04.06 23:20 (59,NE)	05.06 0:08 (62,N)
2456820.573	12.06 0:56 (66,N)	12.06 1:44 (65,N)	12.06 2:33 (64,N)
2456823.413	14.06 21:06 (49,NE)	14.06 21:54 (54,NE)	14.06 22:42 (59,NE)
2456830.513	21.06 23:30 (64,N)	22.06 0:18 (66,N)	22.06 1:06 (65,N)
2456833.353	24.06 19:39 (44,NE)	24.06 20:28 (49,NE)	24.06 21:16 (54,NE)
2456840.453	01.07 22:04 (61,NE)	01.07 22:52 (64,N)	01.07 23:40 (66,N)

6.3   Photometry software

Qatar-1b frames obtained using Holomon observatory equipment were processed with software built for this purpose exactly, photometry of a single target with a transit event, using the python libraries Py-Fits and Num-Py. The steps that are followed by the software are explained in the next paragraphs.

6.3.1   Reduction

The reduction process requires three kinds of reduction frames known as bias, dark and flat.

- Bias are frames with approximately zero exposure time and covered telescope used to correct systematic errors caused by the camera itself such as readout noise. Readout noise consists of two components, the first is the conversion from an analog signal to a digital number, which is not perfectly repeatable and the second is that the electronics themselves will introduce spurious electrons into the process

- Dark are frames with non zero exposure time but also covered telescope used to correct systematic errors caused by the conditions such as thermal noise. In every material, such as silicon in a CCD, at a temperature much above absolute zero electrons are freed from the valence band. These dark current electrons become part of the signal.

- Flat are frames with non zero exposure time picturing a uniform white source of light used to correct systematic errors caused by the geometry of the telescope resulting in an non uniform distribution of light inside it.

From the reduction frames we calculate the master reduction frames:

$$masterbias = \frac{\sum bias_i}{N_{bias}}$$
$$masterdark = \frac{\sum (dark_i - masterbias)/t_{dark_i}}{N_{dark}}$$
$$masterflat = \frac{\sum flat_i - masterbias - t_{flat_i} \times masterdark}{N_{flat}}$$
$$masterflat_{norm} = \frac{masterflat}{mean(masterflat)}$$

(6.1)

Finally every frame is corrected using the formula:

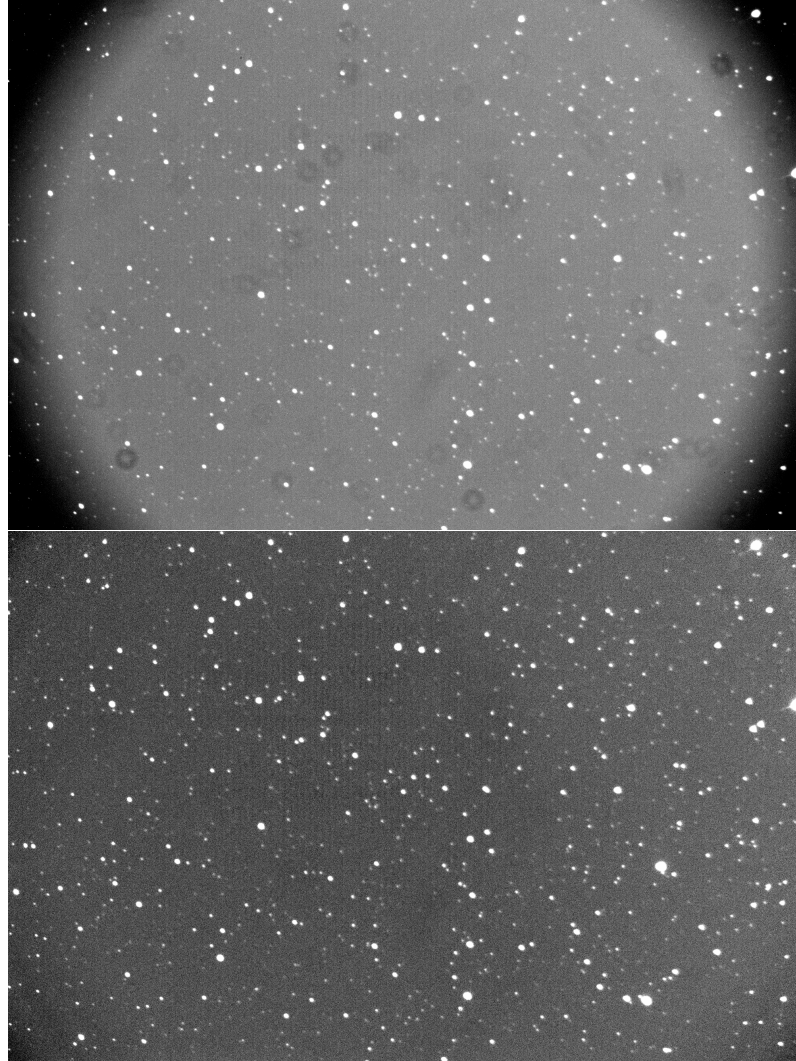$$newframe = \frac{frame - masterbias - t_{exp} \times masterdark}{masterflat_{norm}}$$

(6.2)

Figure 6.6: Qatar-1b field of view before and after reduction.

6.3.2 Alignment

Due to technical problems the frames are not always the same while time passes. The two main reasons for these changes is that a mount is not always tracking very accurately and some mounts (including CGE Pro) need to be rotated when the target crossed the local meridian. For this reason, our software uses the fixed relative positions of stars to find any possible move or rotation of the field of view during the observation. This part of the process is called alignment.

To achieve alignment the software finds some stars, located at (x_i, y_i) in the field of view, quite bright, to use them as reference. Consider one of these, (x_0, y_0), to be the center of a polar coordinate system in which the other stars have polar coordinates (r_i, θ_i). In a next frame (indicated by the letter j) the star-center will be at position $(x_0 + \Delta x_j, y_0 + \Delta y_j)$ and the polar coordinates of the other stars around it will be $(r_i, \theta_i + \Delta \theta_j)$.
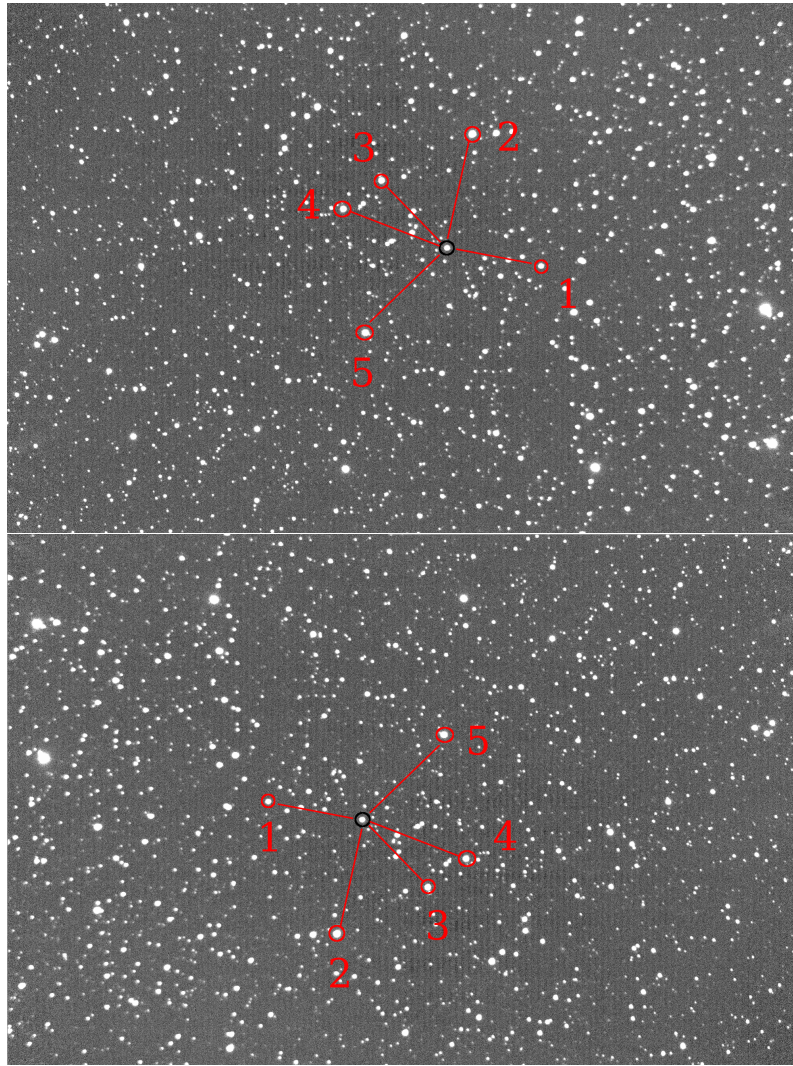

Figure 6.7: Qatar-1b field of view from two different angles. The center star is in a black circle and rest of the reference stars are in red circles and numbered. It is obvious that while the positions and the angle change, the relative positions of the stars are the same.

Assume now that we have the target star initially positioned at (X_0, Y_0), in a following frame our star will be located at:

$$
\begin{aligned}
X &= \Delta x_j + (X_0 - x_0)\cos(\Delta\theta_j) - (Y_0 - y_0)\sin(\Delta\theta_j) \\
Y &= \Delta y_j + (Y_0 - y_0)\cos(\Delta\theta_j) + (X_0 - x_0)\sin(\Delta\theta_j)
\end{aligned}
\tag{6.3}
$$

6.3.3 Photometry

Photometry is the most important part of the whole procedure because it produces the final light-curves. Our software uses aperture photometry but with a changing in shape aperture that we call, pattern photometry. The reason that we had to introduce the pattern photometry is that in many cases the stars in a frame are not circles but their shape can differ due to a variety of reasons (mainly because the mount is not always tracking very accurately). Having the position of the target star in each frame from the alignment part the software picks up all the pixels in its neighbourhood, within a radius defined each time by the user, and construct their distribution. From them, those with counts more than $mean + \sigma$ and closer to the center of the star are considered as part of the pattern. Depending on the number of the pixels in the pattern, a number of nearby sky pixels are collected to calculate the sky value of the neighbourhood. The photometry result is:

$$
\rho_F = N_* - n_{pix}N_S \pm \sqrt{N_* + n_{pix}(N_S + N_D + N_R^2)}
\tag{6.4}
$$

where N_* is the total counts of the n_{pix} pixels inside the pattern and N_S, N_D and N_R are the counts per pixel coming from the sky, the dark current (dark frames) and the read-out noise (bias frames) respectively.

This calculation is simultaneously performed for the target star and for any other star that we want to use as comparison. Comparison stars are necessary for the final output because during a night the atmospheric conditions change and the light from a star is not constant in contrast with the ratio between the light from two (or more) stars. So the final result is:

$$
rel_F = \frac{\rho_{target}}{\sum \rho_{com}} \pm \sqrt{\frac{\sigma_{\rho_{target}}^2}{\left(\sum \rho_{com}\right)^2} + \frac{\rho_{target}^2}{\left(\sum \rho_{com}\right)^4}\sum \sigma_{\rho_{comp}}^2}
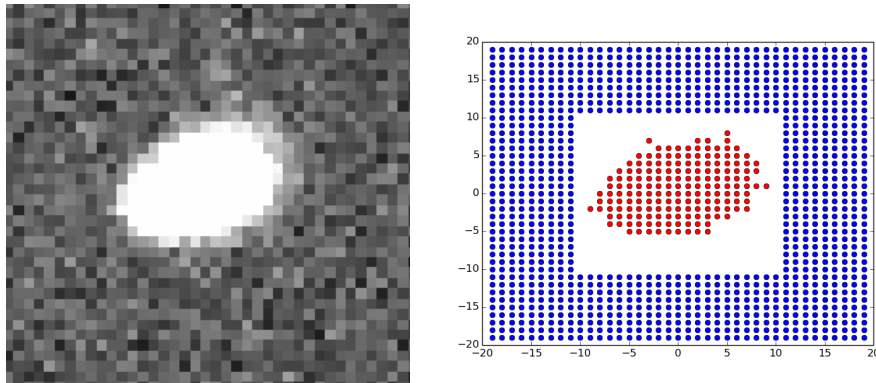\tag{6.5}
$$

Figure 6.8: Qatar-1b pattern (red dots) and sky (blue dots).

6.3.4   Tests

In order to test the reliability of our photometry and fitting software we observed, among others, two known transiting exo-planets, Tres-3b ($RA\,17^h52^m07^s,\quad DEC\,+37^o32'46''$) and HatP-36b ($RA\,1^h33^m04^s,\quad DEC\,+44^o54'55''$) with periods of 1.30618608 and 1.327347 days respectively. The results are presented in the next figures.
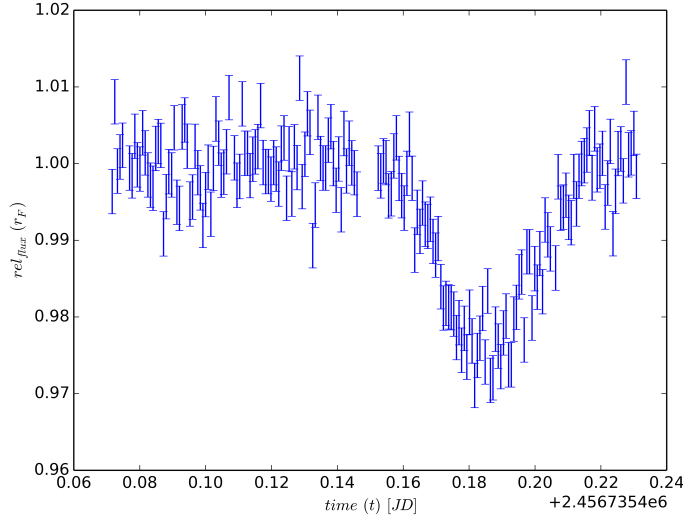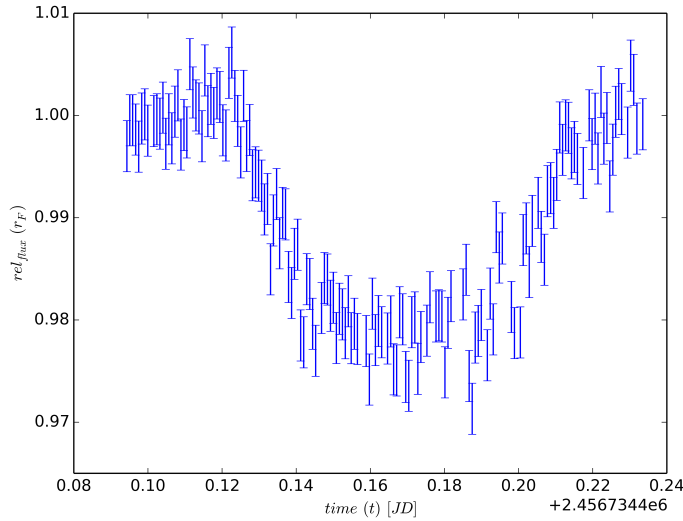

Figure 6.9: Transit of Tres-3b on 18 March 2014.

Figure 6.10: Transit of HatP-36b on 17 March 2014.

As we can see, the rms of the residuals is less than $3mmag$ and it proves that with this equipment and software we are beyond doubt able to observe the transits of Qatar-1b with satisfying accuracy.

6.4   Observations and light-curves

The following figures show the transits of Qatar-1b observed from Holomon observatory. The exposure times were 60 to 90 seconds depending on the conditions and the comparison stars can be seen in the next figure. The light-curves were also de-trended with a second degree polynomial that maybe has caused inaccuracies in inclination and planet radius.
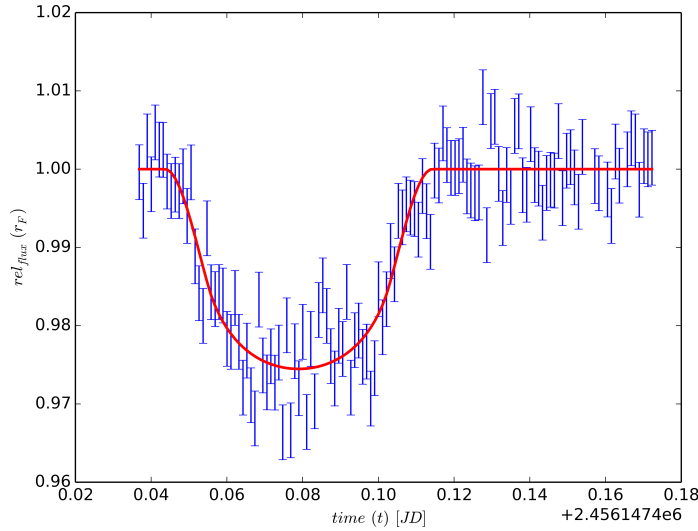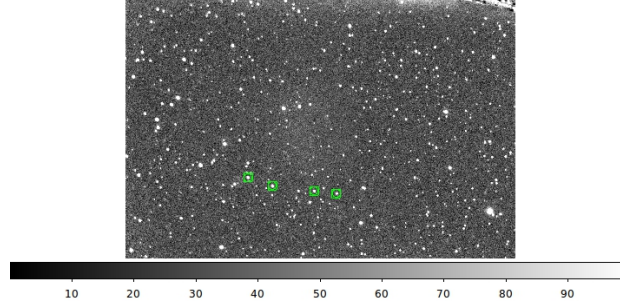

Table 6.4: Fitting results.

parameter	value
mid-transit point	2456147.4789 ± 0.0006
inclination	85.1 ± 0.2
planetary radius	0.142 ± 0.02
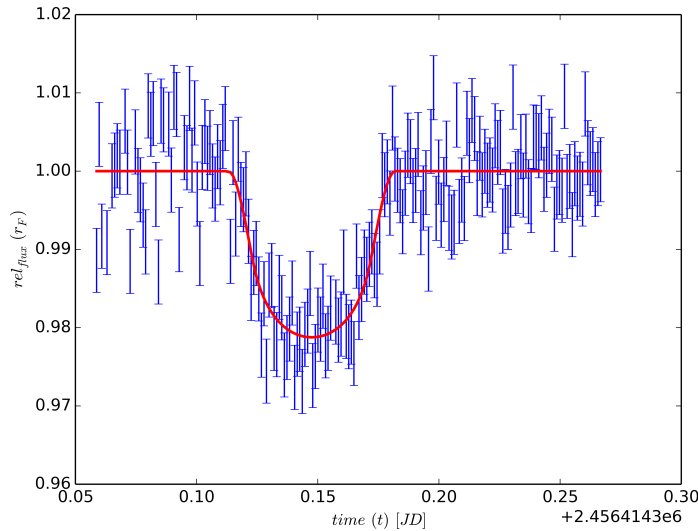
Table 6.5: Fitting results.

parameter	value
mid-transit point	2456414.4475 ± 0.0008
inclination	85.0 ± 0.2
planetary radius	0.130 ± 0.002
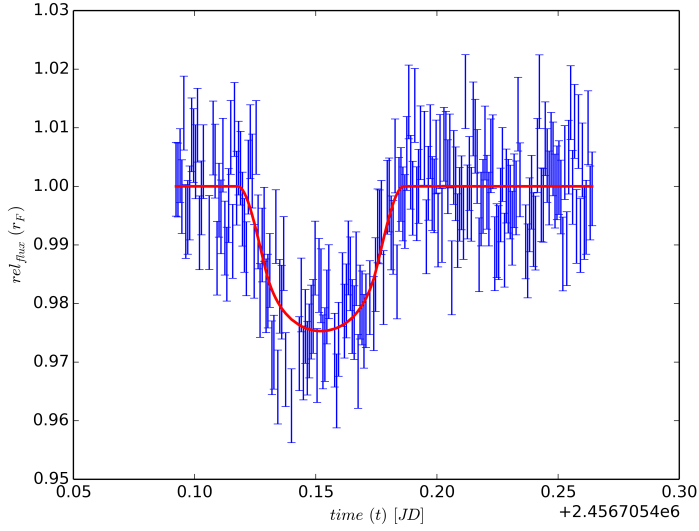
Table 6.6: Fitting results.

parameter	value
mid-transit point	2456705.5521 ± 0.0009
inclination	84.7 ± 0.3
planetary radius	0.142 ± 0.03
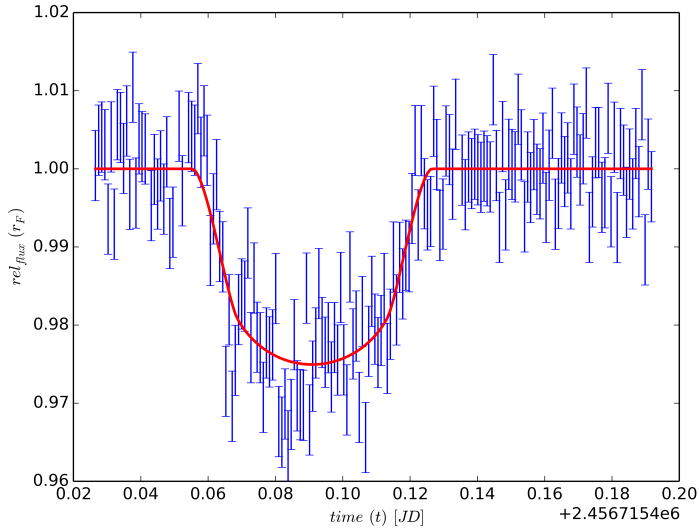
Table 6.7: Fitting results.

parameter	value
mid-transit point	2456715.4909 ± 0.0006
inclination	84.9 ± 0.3
planetary radius	0.149 ± 0.04
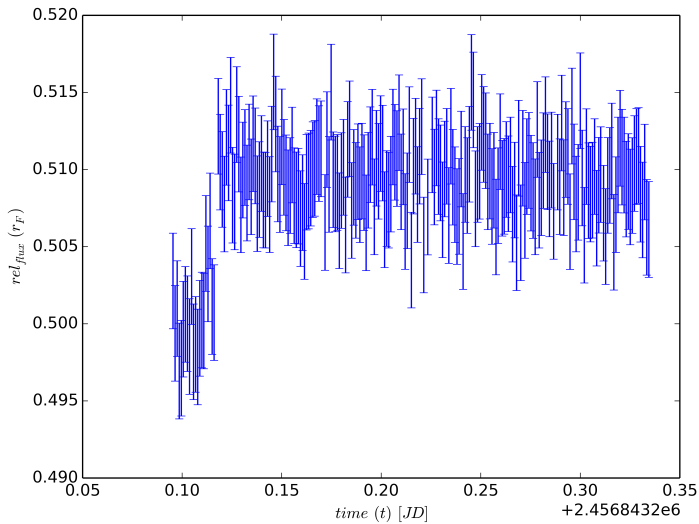
Table 6.8: Fitting results.

parameter	value
mid-transit point	2456843.2894 ± 0.0018
inclination	not fitted
planetary radius	not fitted

6.5 Transit timing variations

We added our results to previous follow up observations (von Essen et al. 2013)
(table 6.9) with no change of course to the previous periodogram as our points were
too few.

Table 6.9: Times of transits.

| transit phase	T_0 [BJD$_{TDB}$-2455500]	OC [days]
previous observation (von Essen et al. 2013)		
-364	140.53449 ± 0.00033	0.00142
-359	147.63337 ± 0.00023	0.00017
-319	204.43373 ± 0.00038	-0.00045
-314	211.53337 ± 0.00079	-0.00093
-288	248.45453 ± 0.00071	-0.00042
-281	258.39446 ± 0.00051	-0.00066
-269	275.43500 ± 0.00037	-0.00041
-250	302.41596 ± 0.00099	0.00007
-226	336.49677 ± 0.00026	0.00030
-83	539.56037 ± 0.00031	0.00037
-81	542.40039 ± 0.00104	0.00035
-76	549.50031 ± 0.00027	0.00014
-43	596.36017 ± 0.00119	-0.00081
-33	610.56044 ± 0.00102	-0.00079
0	657.42192 ± 0.00027	-0.00012
19	684.40315 ± 0.00113	0.00064
31	701.44294 ± 0.00031	0.00014
52	731.26325 ± 0.00029	-0.00007
-121	485.60059 ± 0.00070	0.00153
-69	559.43884 ± 0.00086	-0.00150
-57	576.47921 ± 0.00040	-0.00143
-43	596.35925 ± 0.00084	-0.00173
-31	613.39986 ± 0.00078	-0.00142
-24	623.34079 ± 0.00125	-0.00066
-12	640.38093 ± 0.00045	-0.00081
0	657.42114 ± 0.00093	-0.00090
our observations		
-7	647.48048 ± 0.00059	-0.00101
181	914.44712 ± 0.00078	0.00065
386	1205.55188 ± 0.00091	0.00045
393	1215.49053 ± 0.00061	-0.00062
483	1343.29025 ± 0.00179	-0.00236
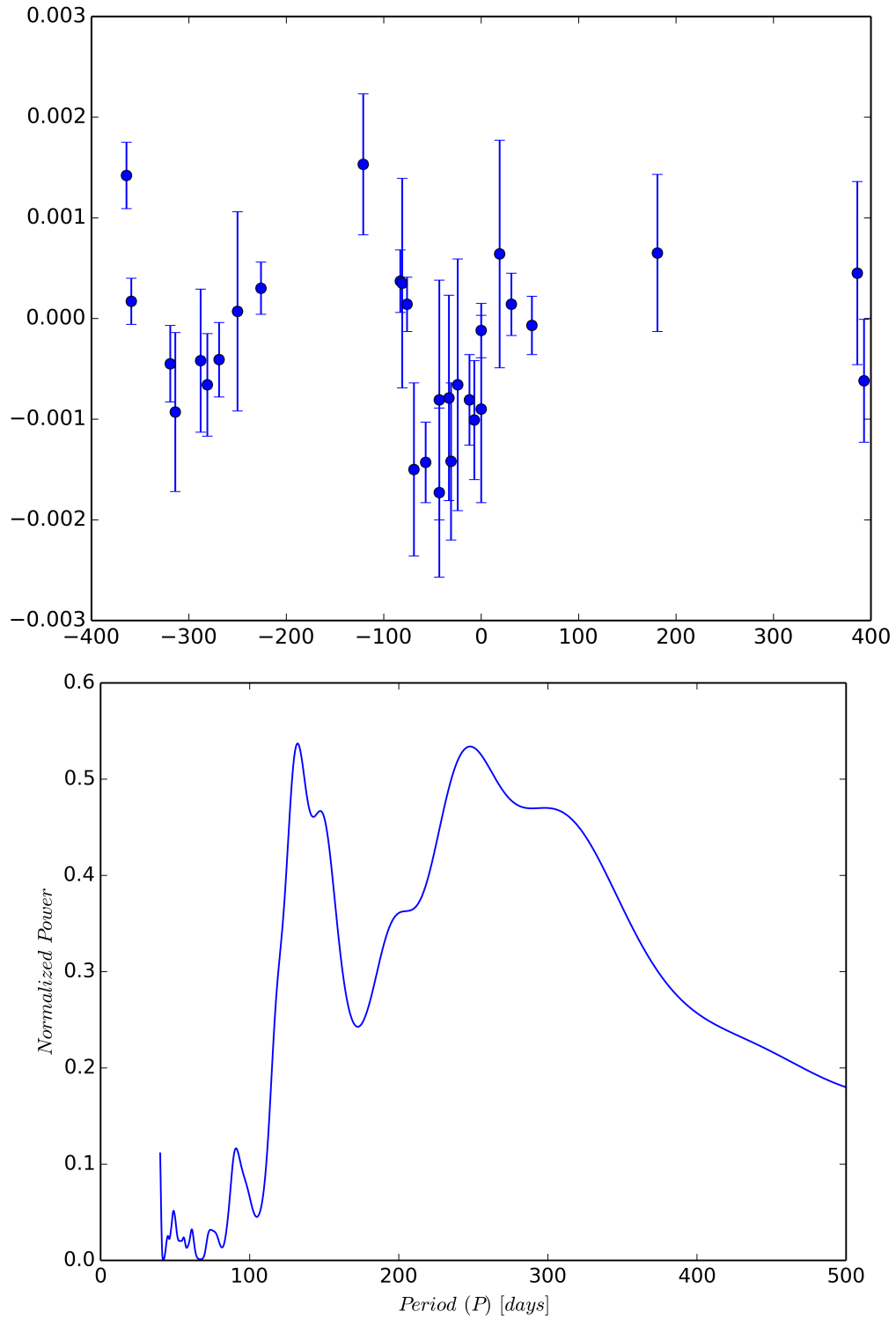
Figure 6.11: O-C diagram (above) and general Lomb Scargle periodogram (Zechmeister &
Kurster 2009) with a peak at 131.752 days.

Bibliography

[1] Agol, E., Steffen, J., Sari, R., & Clarkson, W. 2005, MNRAS, 359, 567

[2] Barros, S. C. C., Díaz, R. F., Santerne, A., et al. 2014, A&A, 561, L1

[3] Bond, I. A., Udalski, A., Jaroszyński, M., et al. 2004, ApJl, 606, L155

[4] Borucki, W. J., Koch, D., Basri, G., et al. 2010, Science, 327, 97

[5] Campbell, B., Walker, G. A. H., & Yang, S. 1988, ApJ, 331, 902

[6] Claret, A. 2000, A&A, 363, 1081

[7] Deming, D., Harrington, J., Seager, S., & Richardson, L. J. 2006, ApJ, 644, 560

[8] von Essen, C., Schröter, S., Agol, E., & Schmitt, J. H. M. M. 2013, A&A, 555,

[9] Gatewood, G., & Eichhorn, H. 1973, AJ, 78, 769

[10] Hatzes, A. P., Cochran, W. D., Endl, M., et al. 2003, ApJ, 599, 1383

[11] Hershey, J. L. 1973, AJ, 78, 421

[12] Hirano, T., Narita, N., Sato, B., et al. 2012, ApJ, 759, L36

[13] Holman, M. J., & Murray, N. W. 2005, Science, 307, 1288

[14] Ioannidis, P., Schmitt, J. H. M. M., Avdellidou, C., von Essen, C., & Agol, E. 2014, A&A, 564, A33

[15] van de Kamp, P. 1963, AJ, 68, 515

[16] Kovács, G., Zucker, S., & Mazeh, T. 2002, A&A, 391, 369

[17] Masuda, K., Hirano, T., Taruya, A., Nagasawa, M., & Suto, Y. 2013, ApJ, 778, 185

[18] Masuda, K. 2014, ApJ, 783, 53

[19] Mayor, M., Queloz, D., Marcy, G., et al. 1995, IAU Circ., 6251, 1

[20] Mazeh, T., Nachmani, G., Holczer, T., et al. 2013, ApJs, 208, 16

[21] Nesvorný, D., Kipping, D., Terrell, D., et al. 2013, ApJ, 777, 3

[22] Pál, A. 2008, MNRAS, 390, 281

[23] Ragozzine, D., & Holman, M. J. 2010, arXiv:1006.3727

[24] Swain, M. R., Vasisht, G., & Tinetti, G. 2008, Nature, 452, 329

[25] Swain, M. R., Vasisht, G., Tinetti, G., et al. 2009, ApJl, 690, L114

[26] Tinetti, G., Beaulieu, J. P., Henning, T., et al. 2012, Experimental Astronomy, 34, 311

[27] Wolszczan, A., & Frail, D. A. 1992, Nature, 355, 145